Hydrogenated Microcrystalline Silicon Thin Films

21

Ying Zhao, Xiaodan Zhang, Lisha Bai, and Baojie Yan

Contents

Abstract

We review μc-Si:H material's properties, deposition techniques, and applications in solar cells. The focus is on the issues that limit μc-Si:H solar cell performance. Because of unintentional impurity incorporation, μc-Si:H shows an N-type conductivity, especially in the early days, μc-Si:H was used only as the doped layers. Meier et al. used VHF-PECVD technique with reduced

---

Y. Zhao · X. Zhang · L. Bai · B. Yan (✉)
Institute of Photoelectronic Thin Film Devices and Technology, Nankai University,
Tianjin, P. R. China
e-mail: zhaoygds@nankai.edu.cn; xdzhang@nankai.edu.cn; baojie.yan@yahoo.com

© Springer-Verlag GmbH Germany, part of Springer Nature 2019

D. Yang (ed.), *Handbook of Photovoltaic Silicon*,
https://doi.org/10.1007/978-3-662-56472-1_28

impurity levels and made first μc-Si:H solar cell in 1994. Since then the research and development of μc-Si:H solar cells have attracted a great attention, and a significant progress has been made for using μc-Si:H as the bottom cell in multijunction structures. Compared to a-Si:H, μc-Si:H structure is much complicated with nanometer sized grains, grain boundaries, amorphous tissues, and microvoids. The complexity in the structure leads to complicated material properties, such as electronic structure, optical absorption, carrier transport, and stability. The material's property affects the solar cell performance significantly. The material structure changes with the film thickness under a constant deposition condition, which influences the solar cell performance. For solar cell applications, it has been found that the best μc-Si:H material should be compact with a low defect density and a crystalline volume fraction around 50% in the whole absorber layer. In order to obtain a high photocurrent density, an effective light trapping is achieved using textured substrates. However, a high textured substrate causes a degradation of material quality. A thick μc-Si:H up to 5 μm requires a high rate deposition. Here, we will discuss the techniques for resolving the μc-Si:H issues and the approaches for achieving the high quality materials and high efficiency μc-Si:H solar cells.

Keywords

μc-Si:H · nc-SiOx:H · Thin film · PECVD · Impurity · Light trapping · p-i-n · n-i-p · Solar cell · Multi-junction

Introduction

Hydrogenated microcrystalline silicon (μc-Si:H) was invented in 1968. It was first made with a remote hydrogen plasma transport method (Veptek and Marecek 1968). Later on, it was found that in plasma enhanced chemical vapor deposition (PECVD) process, when high hydrogen dilution and high RF power were used, the deposited films showed crystal-like structures in their electron scattering pattern and with high conductivity (Usui and Kikuchi 1979). The materials contain crystal grains with the sizes in the range of a few nm and a few tens nm embedded in hydrogenated amorphous silicon (a-Si:H) tissues; therefore, the materials are also called hydrogenated nanocrystalline silicon (nc-Si:H) in the literature. Although some researchers believe that the grains in nc-Si:H are smaller than in μc-Si:H, no clear distinguish between nc-Si:H and μc-Si:H has been made and they are mixed in the literature. Therefore, we used μc-Si:H only in this chapter for consistency. The deposition of μc-Si:H with PECVD uses the same gases as used for a-Si:H deposition with only some differences in the process parameters such as hydrogen dilution, excitation power, pressure, and temperature. Therefore, the μc-Si:H fabrication techniques are compatible with a-Si:H, which is important for solar panel production.

The early stage μc-Si:H materials have very high conductivity with N-type carrier transport, which has been identified as the contribution of unintentional doping by oxygen and/or nitrogen. Therefore, μc-Si:H was mainly used as the N-type and

P-type doped layer in a-Si:H solar cells (Guha et al. 1986; Yang et al. 1997). An important breakthrough of using μc-Si:H as the absorber layer in solar cells was made by Meier et al. at the University of Neuchatel by using Very High Frequency (VHF) PECVD (Meier et al. 1994a, b). Later on they used a gas purifier to reduce the impurity level and improved μc-Si:H material quality and solar cell performance (Meier et al. 1996). Since then, the study of μc-Si:H material property and the research and development of high efficiency μc-Si:H solar cells have got a great attention worldwide, and a significant amount of results has been published in the literature. For reviews, readers may be referred Finger (2010), Guha et al. (2013), Kondo (2003), and Shah et al. (2003). With the great efforts from the thin film silicon photovoltaic (PV) community, the efficiencies of multijunction thin film silicon solar cells and modules with μc-Si:H as the bottom cell absorber layer have been improved steadily with the highest initial cell efficiency of 16.3% (Yan et al. 2011), stable cell efficiency 13.4% (Kim et al. 2013), and stable module efficiency of 12.3% (Cashmore et al. 2016).

From the material structure point view, μc-Si:H is a mixture of crystallites embedded in amorphous tissues. The material structures are much more complicated than a-Si:H and crystal silicon (c-Si). Although a significant amount of studies has been made in the last a few decades, many problems are still unresolved. Here we will not discuss the complicated physics problems with the materials. Instead, we will focus on a few major issues affecting μc-Si:H solar cell performance and the solutions of the problems. The first phenomenon is the so-called crystalline evolution, in which the crystalline volume fraction increases with the film thickness; second the impurity issue and the ambient degradation of μc-Si:H solar cells and light-induced degradations; third the optical property and the light trapping in μc-Si:H solar cells; and fourth, the microcrystalline silicon germanium alloy (μc-SiGe$_x$:H) for extension of absorption to longer wavelength and microcrystalline silicon oxide (μc-SiO$_x$:H) for doped layers. We also address the issues in solar cell design and optimization such as the doped layer and interface layers and finally the high rate deposition of μc-Si:H for solar panel production. Before the discussion of those issues, a brief review the basic properties of μc-Si:H materials is given.

Basic Material Properties of μc-Si:H

Structure Properties of μc-Si:H

Since μc-Si:H is a mixture of crystalline grains and amorphous silicon tissues, the material structures can be characterized by various methods, including X-ray scattering (XRD) spectroscopy, Raman spectroscopy, transmission electron microscopy (TEM), scanning electron microscopy (SEM), atomic force microscopy (AFM), and real time spectroscopic ellipsometry (RTSE). Below, we will discuss some basic observations with these characterizations methods.

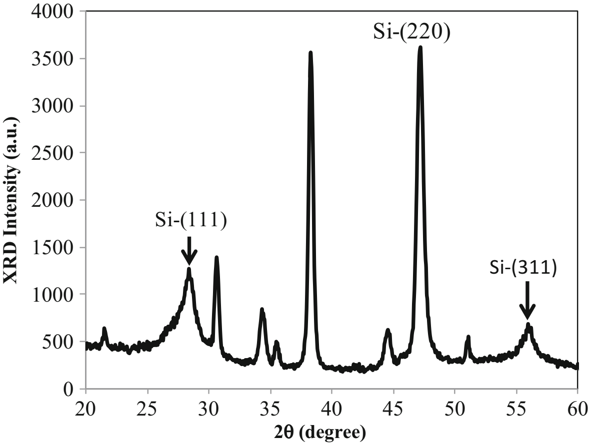

Fig. 1 An XRD pattern of μc-Si:H solar cell deposited on Ag/ZnO back reflector coated SS substrates, where the three crystalline Si peaks are marked and the others unmarked are from the substrate

XRD is one of the commonly used characterization methods for μc-Si:H materials (Ray et al. 2002; Sobajima et al. 2007). Figure 1 shows a typical XRD pattern of a μc-Si:H solar cell made with VHF-PECVD on ZnO/Ag-coated stainless steel (SS) substrate, where the preferential crystalline orientation is the (220) at $2\theta = 47.311°$ and two other peaks at 28.451° and 56.131° corresponding to the (111) and (311) crystalline orientations, respectively. In addition, a few unmarked peaks are from the ZnO/Ag/SS substrate. The crystallite size d and the internal stress η could be estimated by the Debye-Scherrer equation (Debye and Scherrer 1916),

$$\Delta\theta \cos\theta = \frac{k\lambda}{d} + \eta \sin\theta, \tag{1}$$

where λ is the wavelength of the X-ray, θ the scattering angle, $\Delta\theta$ the full width at the half maximum (*FWHM*), and k a constant in the range of 0.8 and 1.39. The commonly used X-ray is the K_α radiation line of Cu with the wavelength of 0.15418 nm. One could plot $\Delta\theta cos(\theta)$ versus $sin(\theta)$ and obtain the internal stress from the slope and the crystallite size from the intersection. In most case, the internal stress is ignored with $\eta = 0$, and the crystalline size is estimated by the Scherrer equation. One should keep in mind that the Debye-Scherrer equation is assumed spherical grain structures. However, in real μc-Si:H materials, the crystallites are elongated perpendicularly to the growth surface, and therefore, the estimated grain size is normally smaller than the real average value. As observed in Fig. 1, the *FWHM* of the (220) peak is narrower than the other two peaks, which indicates that the grains with (220) preferential orientation are larger than the (111) and (311) orientated grains. For most of high quality μc-Si:H materials, the estimated grain sizes from the (220) peak are in the range of 20–30 nm.

Raman spectroscopy is another most commonly used method to analyze μc-Si:H materials (Ledinsky et al. 2006; Vallat-Sauvain et al. 2006a). Because μc-Si:H

Fig. 2 Raman spectra of a μc-Si:H solar cell deposited on a ZnO/Ag back reflector coated SS, where (**a**) is the as measured spectrum with four a-Si:H modes, one c-Si TO mode, and one intermedium component, (**b**) the measured spectrum with baseline correction and the three component fittings

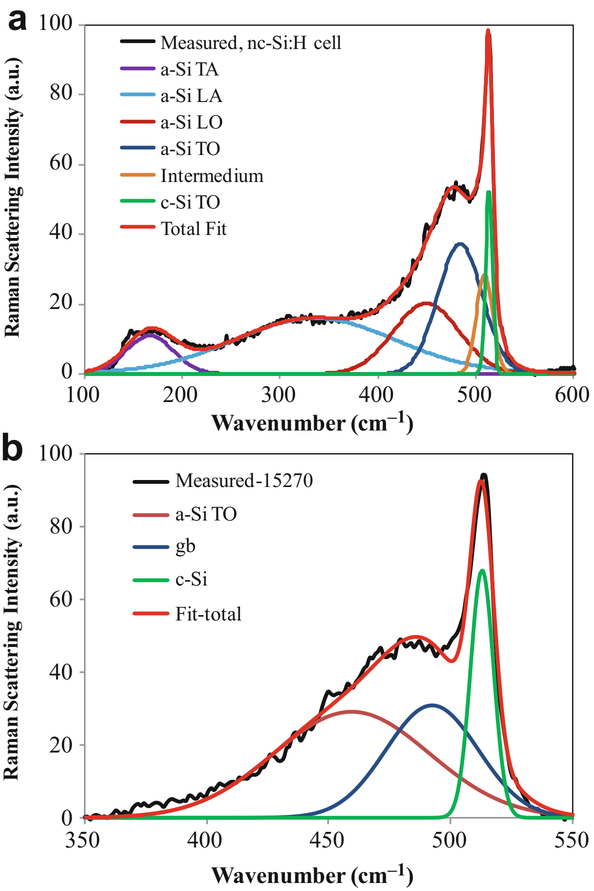

contains crystallites and a-Si:H tissues, roughly speaking its Raman spectrum is a combination of the spectra of a-Si:H and c-Si. The a-Si:H component has four vibration modes of TA, LA, TO, and LO vibrations as shown in Fig. 2a with the deconvolution for the measured spectrum with multiple components. Since the c-Si Raman spectrum has only the TO mode because of the conservation of momentum, the most information of the crystalline structure is in the TO mode, where it is a combination of the amorphous silicon TO mode and the crystalline silicon TO mode with some differences, where the crystalline TO peak broadens and shifts to the low energy side at around 510 − 520 cm^{-1}, the amorphous TO peak narrows and shifts to the high energy side at around 480–490 cm^{-1}. In addition, an intermedium peak at around 500–505 cm^{-1} is observed and normally assigned to the vibration at grain boundaries and the crystallites with the size smaller than 3 nm. From the red shift and the bandwidth of the c-Si peak (Iqbal and Veprek 1982), the grain size could be estimated, but the accuracy is affected by the internal stress and can only be applied to small grains. Therefore, accurate estimations of grain sizes and distributions cannot be obtained by Raman spectra, but can be obtained from cross-sectional TEM images.

The deconvolution of Raman spectra with all of the possible vibration modes is complicated and with a high level of arbitrariness because of the multiple fitting parameters in each component. The commonly used method for the Raman spectral analysis is taking a baseline correction to remove the contributions from the other modes except the TO mode. An example is given in Fig. 2b, where a linear baseline correction is taken in the range of 350 cm^{-1} to 550 cm^{-1}. The baseline corrected spectrum is fitted with three Gaussian curves assigned to the a-Si:H TO mode, the grain boundary TO mode, and c-Si TO mode. Using the three component fitting, the most important structure information of crystalline volume fraction, f_c, is estimated by

$$f_c = \frac{I_c + I_i}{I_c + I_i + mI_a}, \tag{2}$$

where I_c, I_i, and I_a are the integrals of TO modes of c-Si, grain boundary, and a-Si:H, respectively, and m is a correction factor for the Raman cross-sections of amorphous and crystalline phases and its value relates to the size of crystallites d_c,

$$m = 0.1 + \exp\left(-\frac{d_c}{250}\right). \tag{3}$$

However, the real m value is very controversial, and it also depends on the probe light wavelength. Some early published values are in the range from 0.1 to 0.9 (Brodsky et al. 1977; Bustarret et al. 1988; Tsu et al. 1982), but Vallat-Sauvain et al. (2006a) determined that $m = 1.68$ for the measurements with 633 nm red laser and 1.78 for 514 nm green laser. Because of the uncertain of the m value, the absolute crystalline volume fraction may not be able to be determined by Raman measurements, but a relative comparison between samples provides very useful information. In this sense, a simple treatment using $m = 1$ is widely used.

Measured Raman spectra could be also different when using different excitation lasers because of the different absorption coefficients for different wavelengths: a short wavelength probes the top layer of the sample due to a high absorption coefficient, and a long wavelength gives the bulk information due to a nearly uniform absorption. Also the measurements with the illumination on the top surface and on the rear surface of μc-Si:H deposited on a glass substrate can obtain different results because of the crystalline evolution as will be discussed later. Another important factor in real measurement is to keep the light intensity low enough to avoid light-induced crystallization, which easily happens when micro-Raman is performed with a focused laser beam.

Cross-sectional TEM is a direct observation method to measure the structures of μc-Si:H films. Depending on the selection of the resolution, one can study the overall structure and fine structures. Figure 3 presents two TEM images with different resolutions. The left one (Bailat et al. 2002) is taken with a low resolution to examine the structure cross the entire film thickness, where several features are observed with

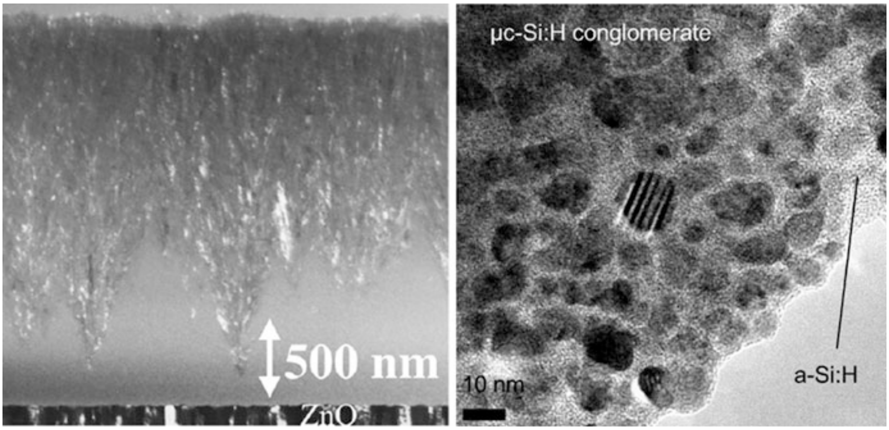

Fig. 3 The left image is a low resolution cross-sectional TEM of a μc-Si:H film on glass (Bailat et al. 2002), and the right one is a high resolution TEM image showing the nanometer sized c-Si grain embedded a-Si:H matrix (Vallat-Sauvain et al. 2006b)

an a-Si:H incubation layer in the bottom smooth area, the formation of crystalline seeds as seen by the spike-like structures, and the growth of the crystalline volume fraction as approaching the top part of the sample. This phenomenon is called “crystalline evolution” and will be discussed in detail later part of this chapter. The right image (Vallat-Sauvain et al. 2006b) is a high-resolution TEM showing nanometer sized nc-Si grain embedded in an a-Si:H tissue. By carefully examining high resolution TEM images, one could obtain the crystallite density, grain size distribution, and compactness of the materials.

AFM is another very useful microscopic analysis tool for μc-Si:H characterization, especially combining the surface morphology mode with conductive mode (Rezek et al. 2002; Yan et al. 2007). Because a-Si:H is normally smoother than μc-Si:H. The formation of large grains, especially the clusters formed with nanometer sized grains, generates higher surface textures than pure a-Si:H. In addition, μc-Si:H has much higher conductivity than a-Si:H; a surface current distribution measured with c-AMF reveals a lot of useful information for microcrystalline formation.

Figure 4 shows a comparison of (a) the c-AFM images and (b) the regular AFM morphology images taken in the same corresponding areas on the surface of an a-Si:H (left one), a mixed-phase Si:H (middle one), and a μc-Si:H (right) samples (Yan et al. 2007). It is observed that the a-Si:H surface is relatively flat with a much lower surface current as shown by the left images. The most interesting observation is from the mixed-phase sample, where the two areas as pointed by the arrows have high mountain-like humps on the morphology image, correspondingly the current is much higher in these areas than the rest of the areas (note the current axis unit is 1 nA). For the μc-Si:H film with a high crystallinity, many mountain-like humps aggregate together and form very rough surface, corresponding, the c-AFM image shows very high current spikes all over the surface (note the current axis unit is 2 nA). These results give a clear picture of the transition from a-Si:H and μc-Si:H.

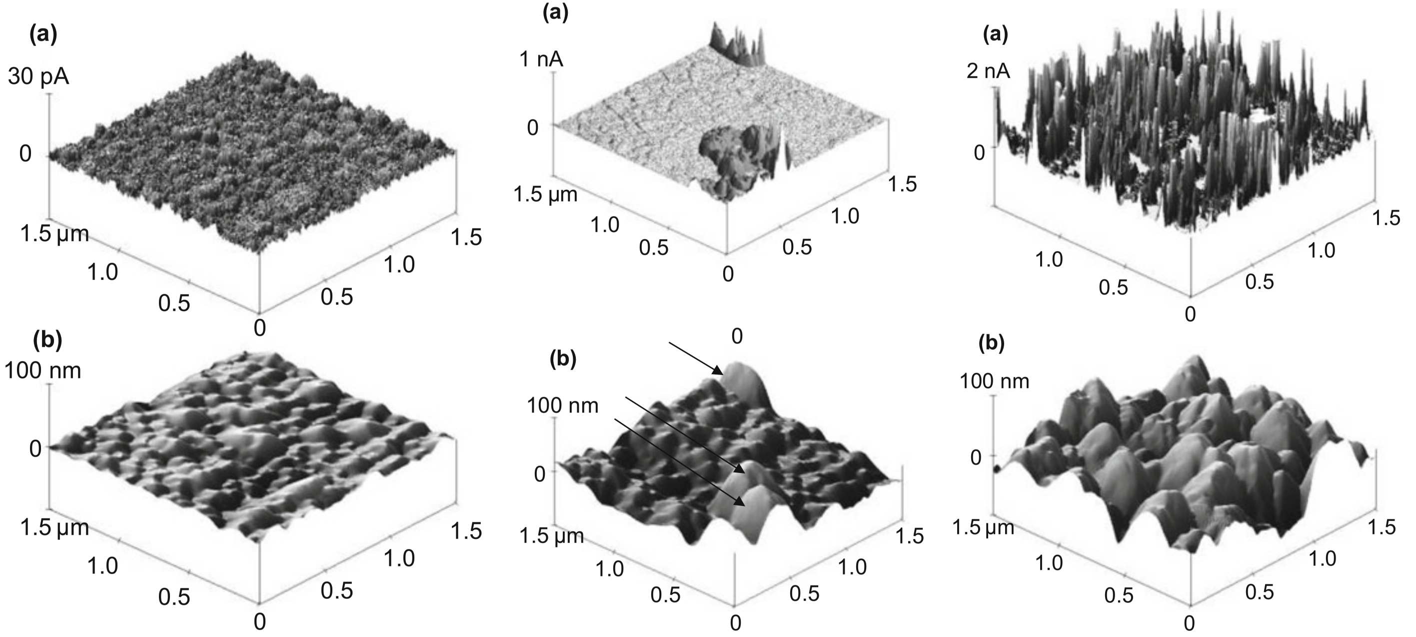

Fig. 4 Regular surface morphology AFM images (bottom) and corresponding c-AFM images (top) in the same areas for an a-Si:H (left), a mixed-phase (middle), and a µc-Si:H (right) samples (Yan et al. 2007)

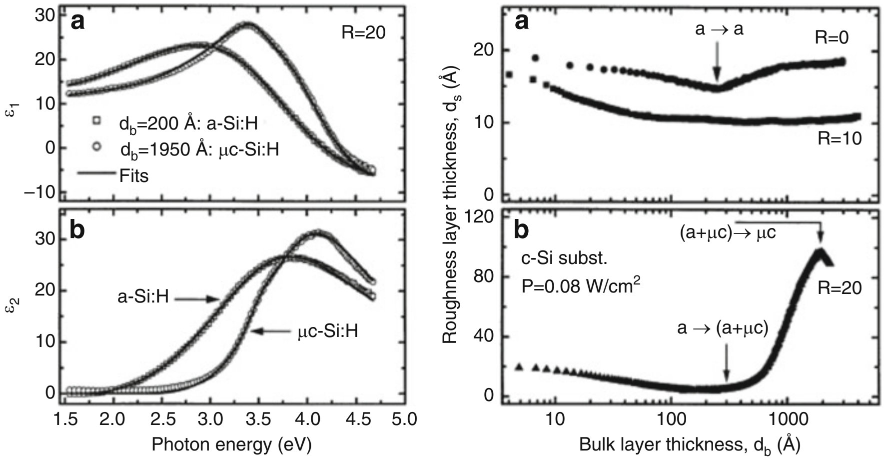

Fig. 5 Left panel: (**a**) Real ε_1 and (**b**) imaginary ε_2 parts of the dielectric functions at 200 °C for the R = 20 Si:H film at the bulk thickness of 20 nm and 195 nm, right panel: surface roughness layer versus the bulk layer thickness for three samples with different hydrogen dilution R (Collins et al. 2003)

Real-time spectroscopic ellipsometry (RTSE) is also widely used for a-Si:H and μc-Si:H characterization, especially the transition from a-Si:H to μc-Si:H. By analyzing measured real and imaginary parts of the dielectric functions of a thin film versus photo-energy, the bulk thickness and surface roughness can be obtained. Reviews of RTSE and details of the analyses can be found in Ref. Collins et al. (2003) and Dahal et al. (2014).

Figure 5 shows an example of measurement and analysis results, where the left plots are the measured real and image parts of the dielectric function spectra for the deposition with hydrogen dilution ratio R = 20 (H_2/SiH_4) at 200 °C at two thickness of 20 nm and 195 nm, and the right plot gives the analysis results of the surface roughness as a function of bulk layer thickness for three deposition processes with hydrogen dilution ratios R of 0, 10, and 20. By systematic measurements and analyzing different deposition processes, the transition model from a-Si:H to μc-Si:H has been built (Collins et al. 2003), which gives a very useful guideline for μc-Si:H material and device optimizations.

Electronic Properties of μc-Si:H

Dark- and photo-conductivities are critical parameters for solar cell applications. The absorber layer needs to have a low dark conductivity, a high photo-conductivity, and hence a high photosensitivity. Because of the inclusion of crystalline phase, the dark-conductivity of μc-Si:H is higher than of a-Si:H and it increases with the increase of crystalline volume fraction. Figure 6 gives examples of dark- and photo-conductivities as a function of silane concentration ($SiH_4/(SiH_4 + H_2)$) in the deposition process (Vettea et al. 2002). It shows that both the dark- and photo-

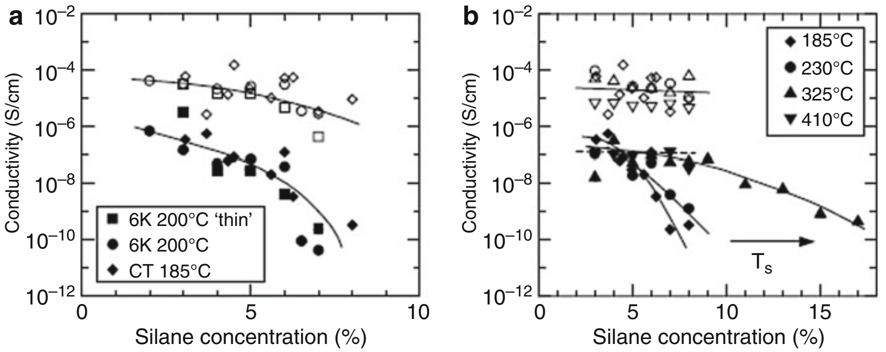

Fig. 6 Dark-conductivity (filled symbols) and photo-conductivity (open symbols) of films prepared at various silane concentrations. (**a**) Results for similar substrate temperatures of 200 °C and 185 °C in two different deposition systems, also including a series with a reduced thickness of 50–100 nm ("thin"). (**b**) Substrate temperature dependent results. Measurement error is within marker size (Vettea et al. 2002)

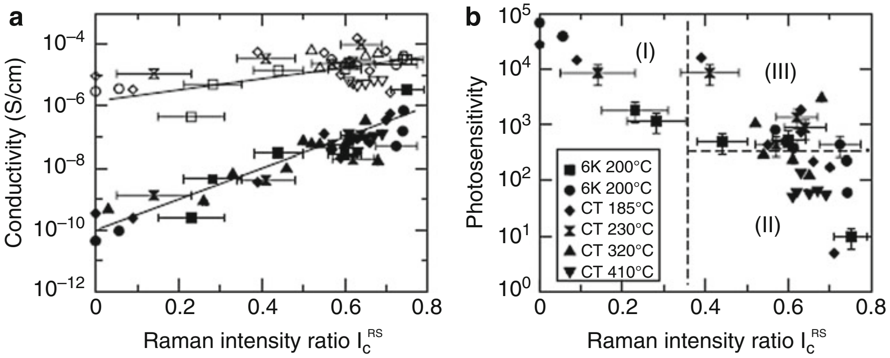

Fig. 7 (**a**) Dark-conductivity (filled symbols) and photo-conductivity (open symbols) as a function of integrated Raman intensity ratio I_C^{RS}, (**b**) photosensitivity as a function of I_C^{RS}. Same symbols are used in both figures. For better readability, only exemplary error bars are included (Vettea et al. 2002)

conductivity increase with the decrease of silane concentration. As will be discussed later, high hydrogen dilution (low silane concentration) promotes the formation of microcrystalline phase. Therefore, conductivity is related to the material structure. Figure 7 (a) plots the dark- and photo-conductivities and (b) the photosensitivity as a function of crystalline volume fraction from the Raman measurement (Vettea et al. 2002). It shows that both the dark- and photo-conductivities increase with the increase of crystallinity, but the photosensitivity decreases with the increase of crystallinity. The dark-conductivity increases from 10^{-11} $(\Omega\text{cm})^{-1}$ of a-Si:H to 10^{-6} $(\Omega\text{cm})^{-1}$ of high crystallinity μc-Si:H by 5 orders of magnitude, while the increase of photo-conductivity is much slower than the dark-conductivity by only

Fig. 8 Arrhenius plot of parallel conductivity (DC) (parallel to the substrate) and perpendicular conductivity (AC) (perpendicular to the substrate) measured on the μc-Si:H sample with 2.2 mm thickness (Kocka et al. 2003)

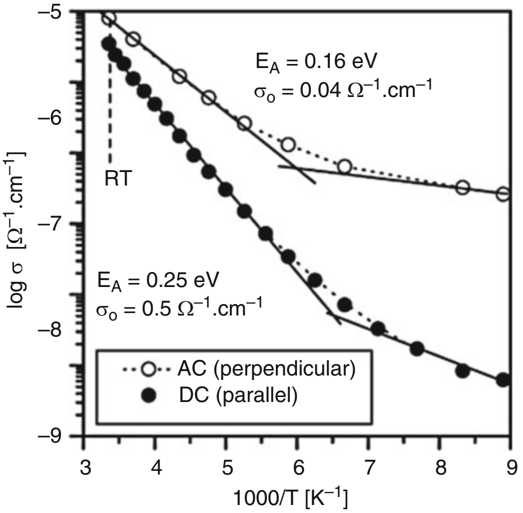

one order of magnitude, which results in the decline of photosensitivity with the increase of crystallinity.

The conductivity of μc-Si:H materials is anisotropy, which means that it is different between the directions of parallel and perpendicular to the film surface with a much higher conductivity in the perpendicular than the parallel directions. This is caused by the unique material structure with crystalline columnar structures perpendicular to the substrate. Even with a smaller crystalline volume fraction than the percolation threshold, the crystalline columnar structure can form perpendicular transport paths for current flow. Figure 8 shows a comparison of perpendicular conductivity (AC) and parallel conductivity (DC) as a function of inverse temperature, indicating a much higher conductivity and lower activation energy in the perpendicular direction than in the parallel direction (Kocka et al. 2001, 2003). With a simple mind thinking, if μc-Si:H has columnar structured nanocrystalline clusters perpendicular to the substrate, the crystalline phase is easy to form transport path for current flow, while the carrier transport in the parallel direction needs go over the amorphous tissues and the grain boundaries.

The anisotropy conductivity of μc-Si:H has a significant impact on solar cell design and fabrication where the carrier transport is in the perpendicular direction, while the commonly used conductivity measurement with two parallel electrodes deposited on the sample surface does not give the real transport properties in solar cells. In addition, the parallel conductivity might be dominated by the high conductive layer on the top surface, while the perpendicular conductivity might be influenced by the low conductive a-Si:H incubation layer. Therefore, the optimization of μc-Si:H materials for solar cell application needs to carefully consider the perpendicular transport. The anisotropy conductivity of μc-Si:H has some advantages, especially in the doped layers. The high perpendicular conductivity with a low crystallinity allows enough conductances for the current flow, but the low parallel conductivity prevents the lateral collection to improve the open circuit voltage (V_{oc}) and fill factor (FF).

For solar cell application, the most important transport parameter is the hole mobility-lifetime product, which limits the collection length of carriers and hence the maximum cell thickness allowing to have enough short circuit current density (J_{sc}) without significant loss in FF. Time-of-flight (TOF) measurements found that the hole drift mobility in a-Si:H is normally in the order of 0.01 cm^2/Vs (Gu et al. 1994), while it increases by two orders of magnitude to the level of 1 cm^2/Vs (Dylla et al. 2005). The high hole mobility allows to use much thicker absorber layer in μc-Si:H solar cells (3–5 μm) than in a-Si:H solar cells (0.2–0.3 μm).

Optical Properties of μc-Si:H

The advantage for using μc-Si:H as the intrinsic layer in solar cell is absorbing the long wavelength light for high J_{sc}; therefore, a high absorption coefficient (α) at the long wavelength is an important signature of μc-Si:H. Figure 9 shows an example of the comparison of measured absorption coefficients of μc-Si:H, intrinsic a-Si:H, and c-Si, from which a few observations are made (Shah et al. 2003). First, comparing to a-Si:H, μc-Si:H has a significant high absorption coefficient in the energy below the a-Si:H bandgap, proving the advantage of μc-Si:H for the long wavelength absorption in solar cell application. Second, the absorption coefficient spectrum of μc-Si:H has a similar shape as of c-Si but with much higher values. It has been confirmed that the measured high absorption is caused by the scattering of the rough surface and the internal scattering by the grain boundaries in the films. The scattering effects can be removed and the measured absorption coefficients are reduced. Figure 10 shows a

Fig. 9 Effective absorption coefficient spectra of as measured μc-Si:H, c-Si, and intrinsic a-Si:H materials (Shah et al. 2003).

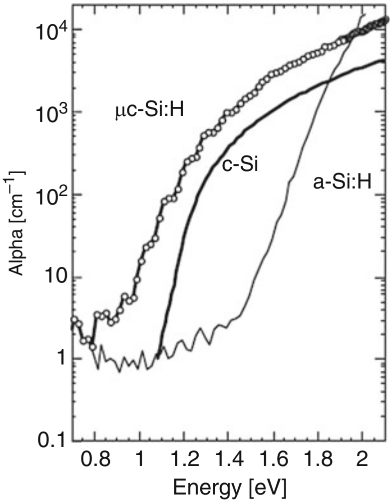

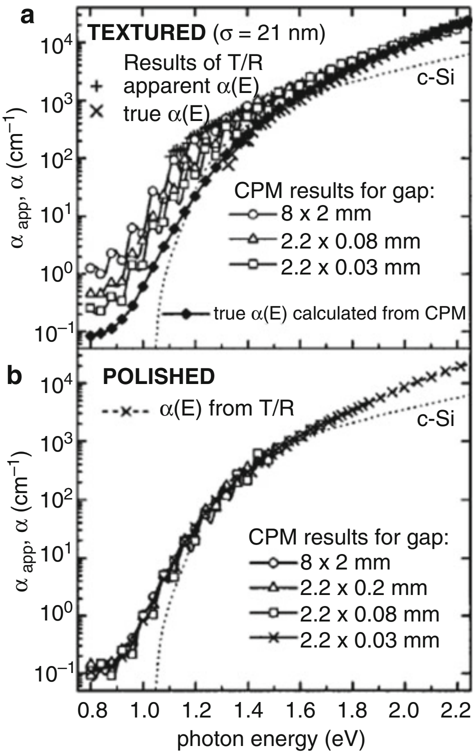

Fig. 10 Apparent optical absorption coefficients of a μc-Si:H sample measured by CPM with different interelectrode spacing (gap) and calculated from T/R measurements: (**a**) in the as-grown state (textured sample) and (**b**) after a chemomechanical polishing. The evaluated spectral dependence of the true absorption coefficient α(E) is shown as the main result by full diamonds; α(E) of crystalline silicon is shown for comparison. The value of the RMS surface roughness of σ = 21 nm of the as-grown sample was evaluated from the T/R data (Poruba et al. 2000)

careful study of removing the scattering effect to obtain the true absorption coefficient spectra in μc-Si:H. The measurements were made with the regular transmission (T) and reflection (R) spectra and constant photocurrent method (CPM) (Poruba et al. 2000), where (a) plots the apparent results with different electrode gaps that affects the scattering effect and the true absorption coefficients by modeling the results to remove the scattering effect, and (b) is the results from a polished sample with different gaps showing the same results without the influence from the scattering. Comparing the results in Fig. 10 (a), one can see that the scattering indeed affects the apparent absorption significantly, especially the long wavelength region, where the low absorption coefficients require a long path for the light to be absorbed. Although the scattering effect leads to a great challenge to obtain the true absorption coefficients, from solar technology point of view, the enhanced absorption by scattering is an important feature for solar cell application because it allows using a much thinner absorber layer than c-Si solar cells. Third, the true absorption coefficients of μc-Si:H in the energy higher than the bandgap of a-Si:H are much higher than in c-Si, which is due to the contribution of the a-Si:H phase; it is also higher than in c-Si in the energy lower than the c-Si bandgap, which results from the absorption in the tail states in μc-Si:H. The absorption coefficient of μc-Si:H does not go down to zero in the energy below the bandgap of c-Si:H at 1.12 eV. This does not

Fig. 11 Optical absorption of the a-Si:H and μc-Si:H films prepared at different silane concentrations as indicated in the figure. For comparison, the absorption of monocrystalline silicon is added (Kroll et al. 1998).

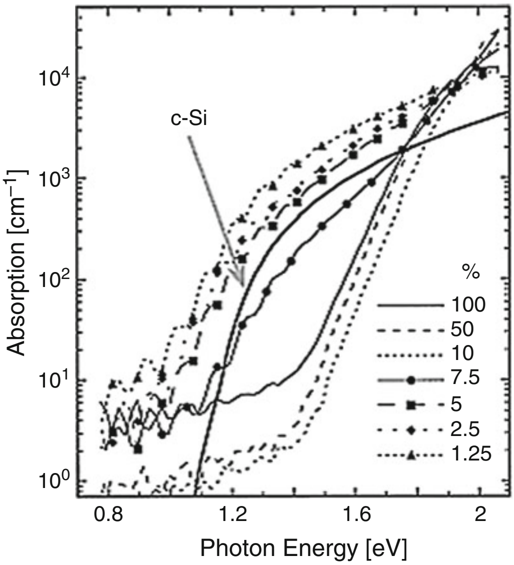

mean μc-Si:H has a narrower bandgap than c-Si, instead indicates a band-tail absorption as the case of a-Si:H.

Logically thinking, the absorption spectrum of μc-Si:H should depend on the crystalline volume fraction with the higher the crystalline volume fraction, the higher the long wavelength absorption is. This trend has been observed experimentally as shown in Fig. 10 (Kroll et al. 1998), where the absorption coefficient spectra of μc-Si:H films made with different silane concentrations for achieving different crystalline volume fractions. It demonstrates that the absorption coefficient at photon energy below the a-Si:H bandgap of ~1.8 eV increases significantly but decreases slightly at above ~1.8 eV. The increases of the low energy absorption coefficients with the reduction of silane concentration are due to the increases of the absorption in the crystalline phase and the increased scattering effect; the slight reductions of absorption in the high energy region result from the reduced a-Si:H component (Fig. 11).

There was a confusion concept about the bandgap of μc-Si:H. Because it has normally observed that the V_{oc} of μc-Si:H solar cells increases with the decrease of crystallinity (Droz et al. 2004). Logically one would expect the bandgap of μc-Si:H increases with the decrease of the crystallinity. But it might not be true. First, the definition of bandgap is the energy between the conduction band edge E_c and the valence band edge E_v. It should be no energy states between E_c and E_v in the ideal case. Since μc-Si:H is a mixture of amorphous tissues and c-Si grains, the definition of the bandgap is sometime confusion and ill-defined. First, the areas of c-Si phase should have the same bandgap as c-Si bulk materials without considering the quantum confinement, while the areas of amorphous phase should have the similar optical properties as a-Si:H. For the μc-Si:H materials used in solar cells, the crystalline phase must form a transport path and the carrier transport mainly takes place in the c-Si phase; therefore, the transport or mobility bandgap of the μc-Si:H

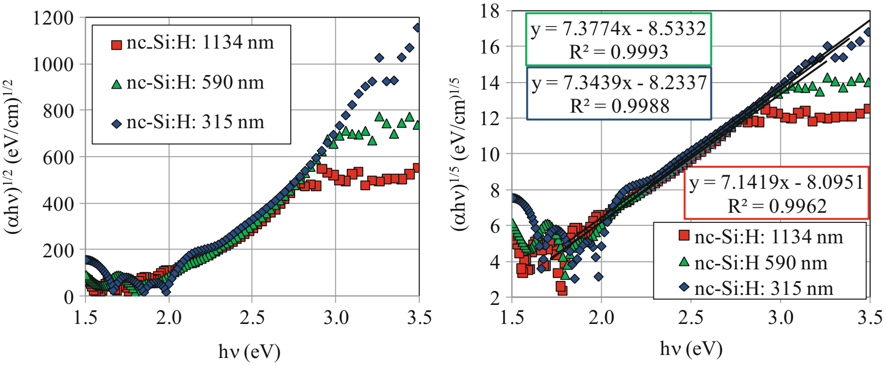

Fig. 12 (left): the Tauc plot of $(h\nu\alpha)^{1/2}$ versus $h\nu$, and (left): $(h\nu\alpha)^{1/5}$ versus $h\nu$ of three μc-Si:H films with different thicknesses made under the same condition

should be the same as c-Si of 1.12 eV. By analyzing the dark current-voltage characteristics of μc-Si:H solar cells, Yan et al. (2013) proved that the mobility bandgap of μc-Si:H is indeed the same as c-Si. Therefore, when considering the carrier transport in μc-Si:H, one should only consider the bandgap of c-Si phase with the same value of 1.12 eV. The optical bandgap does not have a unified definition for the mixed-phase materials. For a-Si:H, the optical bandgap is normally defined by the linear Tauc plot of $(h\nu\alpha)^{1/2}$ versus $h\nu$; Yan et al. (2013) also showed that the Tauc plot of $(h\nu\alpha)^{1/2}$ versus $h\nu$ does not have a good linear relation as given in Fig. 12; instead the $(h\nu\alpha)^{1/5}$ versus $h\nu$ yields a linear relation and gives an intersection at around 1.2–1.3 eV. However, it is difficult to find out an acceptable physics to explain such relation. Therefore, the optical bandgap is difficult to be obtained by the Tauc plot. The curvature in the Tauc plot can be explained with effective medium theory by the composition of the absorption coefficient spectra of a-Si:H and c-Si with a given crystalline volume fraction as shown in Fig. 13 (Yan et al. 2013). It is obvious that combing the two absorption spectra with different bandgaps does not obtain a straight line in the Tauc plot. It is also often to use the energy at which the absorption coefficient is 10^4 cm^{-1} as the definition of optical bandgap (E_{04}), but the E_{04} is sometimes misleading as shown in Fig. 13, where the E_{04} of c-Si is larger than the E_{04} of μc-Si:H and the E_{04} of μc-Si:H is larger than the E_{04} of a-Si:H. Therefore, the E_{04} in μc-Si:H may not give the information of the optical bandgap.

To summarize the optical properties of μc-Si:H, we may conclude that the absorption coefficients of μc-Si:H can be composited by combining the spectra of c-Si and a-Si:H with a given crystalline fraction. Therefore, the absorption coefficient in the high energy region decreases and in the low energy region increases with the increase of crystalline volume fraction. The mobility bandgap in μc-Si:H is the same as in c-Si when carrier transport takes place in the crystalline phase, but the optical bandgap does not have a clear definition yet. The measured absorption coefficients of μc-Si:H could be much larger than the real ones because of the

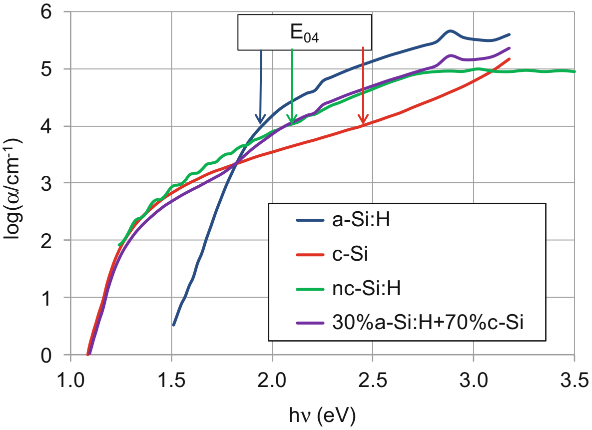

Fig. 13 Absorption coefficient spectra of μc-Si:H, c-Si, a-Si:H, and a combination of 30% of a-Si:H and 70% of c-Si (Yan et al. 2013)

scattering by the rough surface or the internal grain boundaries, which is an important feature for μc-Si:H allowing to use much thinner absorber layer in solar cells.

Application of μc-Si:H in Solar Cells and Issues for Efficiency Improvement

The fabrication of high quality μc-Si:H materials and efficient solar cells has been facing numerous challenges. First the material structure is not uniform along the growth direction when a constant deposition condition is used; the materials show an initial a-Si:H incubation layer and the crystallinity increases with the film thickness, which is called "crystalline evolution" and has a significant impact on solar cell optimization. Second, μc-Si:H films made with no intentional doping normally contain a high concentration of impurity that results in 10^{17} cm^{-3} donors, which leads to the Fermi level close to the conduction band edge and therefore with a low activation energy, a high dark conductivity, and a low photoresponse. This high conductive μc-Si:H cannot be used as the absorber layer in solar cells. The third challenge is to make compactly structured μc-Si:H materials to avoid the postdeposition impurity diffusion. It has been often found that a high density of microvoids and microcracks in μc-Si:H materials made under unoptimized conditions, especially at high deposition rates. The microvoids and microcracks are mainly at the grain boundaries in the samples with a high crystalline volume fraction, where the grain boundaries between large grains are difficult to be passivated. The fourth challenge is the required thickness of μc-Si:H intrinsic layer in solar cells. For an a-Si:H solar cell, the intrinsic layer is normally in the range of 200–300 nm, but it requires approximately ten times more thicker in a μc-Si:H solar cell. Although the long wavelength absorption in μc-Si:H is higher than in a-Si:H, it is still an indirect bandgap in the crystalline phase and the absorption coefficient is not high enough to absorb sufficient long wavelength light with a thin μc-Si:H layer. Normally the intrinsic μc-Si:H layer needs to be 2–3 μm thick and even up to 5 μm. Although it is significantly thinner than a wafer used in c-Si solar cell, it is much thicker than the intrinsic layer in a-Si:H solar cells. Consequently, the deposition rate of μc-Si:H should be approximately 10 times higher than the deposition rate of a-Si:H for reaching the same production rate of thin film solar modules as using a-Si:H and a-SiGe intrinsic layers. For this consideration, the target deposition rate should be 2–3 nm/s for μc-Si:H in thin film silicon solar panel production. Below we will address these issues and approaches to resolve these issues for high efficiency μc-Si:H solar cells.

Crystalline Evolution and Hydrogen Dilution Profile

As mentioned above, the key technique for depositing μc-Si:H is the high hydrogen dilution. Using a PECVD system, on can make a-Si:H and μc-Si:H with different deposition conditions such as high hydrogen dilution, high excitation power, and high pressure. The most effective parameter controlling the amorphous/microcrystalline transition is the hydrogen dilution ratio defined as $R = H_2/SiH_4$ or the silane concentration defined as $SC = SiH_4/(H_2 + SiH_4)$. Figure 14 shows an example of XRD patterns of Si:H films deposited with different SC (Kroll et al. 1998). It notes

Fig. 14 XRD spectra of Si:H films made with different silane concentrations (Kroll et al. 1998)

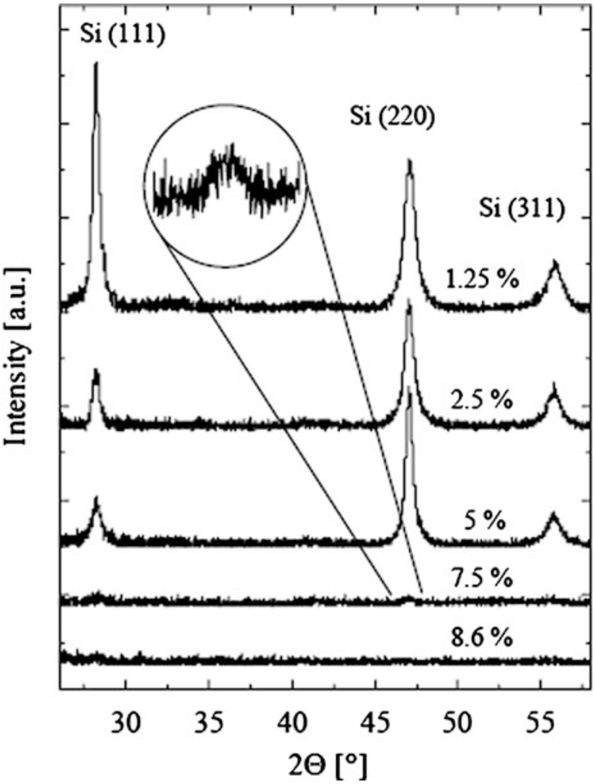

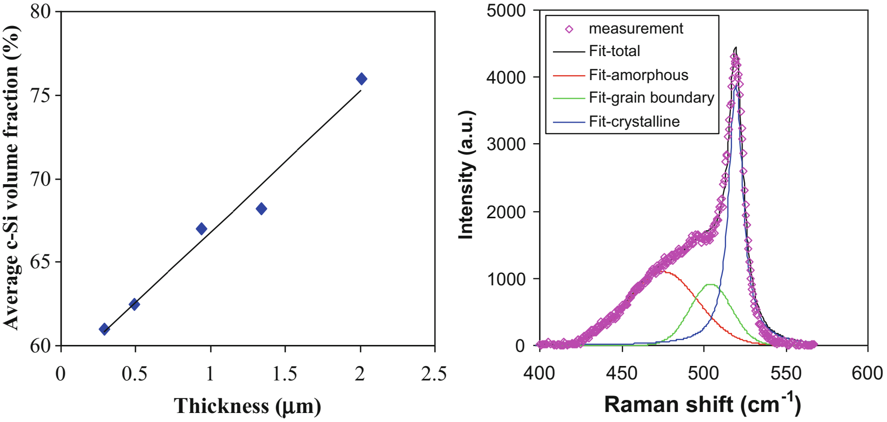

Fig. 15 (right): A Raman spectrum of µc-Si:H film with three component fittings after a linear baseline correction; (left) crystalline volume fraction as a function of film thickness (Yan et al. 2004a)

that the film made with 8.6% of silane shows no any indication of c-Si peaks, 7.5% with an indication of c-Si formation with the (220) preferential orientation peak as observed in the enhanced scale, and the c-Si peaks increase with the decrease of silane concentration. The films made with 5% and 2.5% show a strong (220) preferential orientation, while the (111) peak becomes stronger than the others in the sample with 1.25% silane concentration. This result clearly proves that the hydrogen dilution is an effective parameter to control the crystallinity in µc-Si:H materials.

Another interesting phenomenon in µc-Si:H deposition is the so-called crystalline evolution as shown in Fig. 15a, where the crystalline volume fraction increases with the film thickness increase when the deposition is made under a constant condition. The crystalline volume fraction is measured by the Raman spectra as shown in Fig. 15b with three component fittings (Yan et al. 2004a) as discussed previously with $m = 1$. The Raman measurements were made with Ar ion laser with the wavelength of 514 nm, which only probes the top layer of the samples.

Collins et al. have done a systematic study about the transition from a-Si:H to µc-Si:H and the crystalline evolution with the comparison of cross-sectional TEM and RTSE (Collins et al. 2003; Dahal et al. 2014). Figure 16 shows an example of cross-sectional TEM, where one could observe (1) a clear cone structured crystalline phase formed with a cone angle θ and (2) a crystallite seed density N_d after an a-Si:H incubation layer deposition (Collins et al. 2003). The cone growth with the film thickness agrees well with the increase of crystallinity with film thickness.

On the same sample, RTES was measured and analyzed to obtain the crystallinity with the result shown in Fig. 17 (Collins et al. 2003), in which the crystallinity increases starting from around 30 nm of the a-Si:H incubation layer. Based on this analysis, a cone growth structure model is built as shown in Fig. 18 (Collins et al. 2003). It includes three zones: (I) the a-Si:H incubation layer, (II) the cone growth zone, and (III) the zone after the cone coalescence. In zone I, the crystalline volume

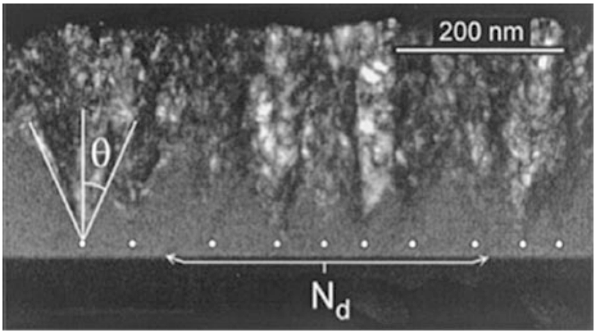

Fig. 16 A cross-sectional TEM image of a μc-Si:H film made with hydrogen dilution R = 20. A clear-cone structured crystalline phase formed with a cone angle θ and crystallite seed density N_d (Collins et al. 2003)

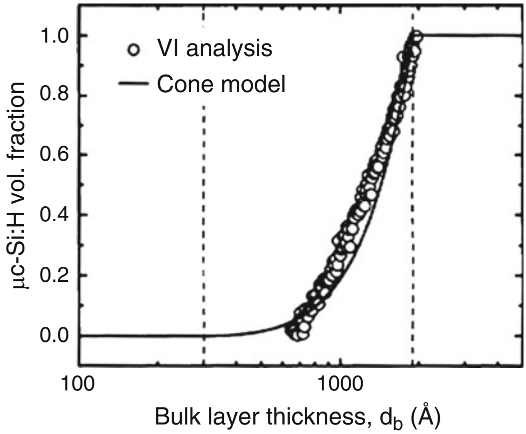

Fig. 17 Crystalline volume fraction estimated from the RTSE analysis as a function of film thickness. The crystalline formation starts from around 30 nm (Collins et al. 2003)

fraction is undetectable and the surface roughness slightly decreases due to the coalescence of the amorphous islands; in zone II, the crystalline volume fraction and the surface roughness both increase with the film thickness due to the growth of the cones; and finally in zone III, the crystalline volume fraction reaches 100% and the surface roughness starts to decrease due to the coalescence of the crystalline cones. It needs to point out that the estimated crystalline volume fractions by RTSE are normally larger than the estimations from Raman spectra.

Based on this RTES analysis, a phase diagram was built up as shown in Fig. 19 (Collins et al. 2003), where the horizontal axis is hydrogen dilution R, and vertical axis the bulk film thickness. Three transitions between four zones are identified as the amorphous unstable surface zone to amorphous stable surface zone transition (a→a), amorphous stable surface zone to mixed-phase zone transition (a→a + μc), and mixed-phase zone to microcrystalline phase zone (a + μc →μc). Details of the analyses and the meaning of each zone and transition are referred to Ref. Collins et al. (2003). This phase diagram is a very useful tool for guiding the design and optimization of thin film solar cells. It has been found that the best a-Si:H solar cells are made at a high hydrogen dilution close to the transition from amorphous to

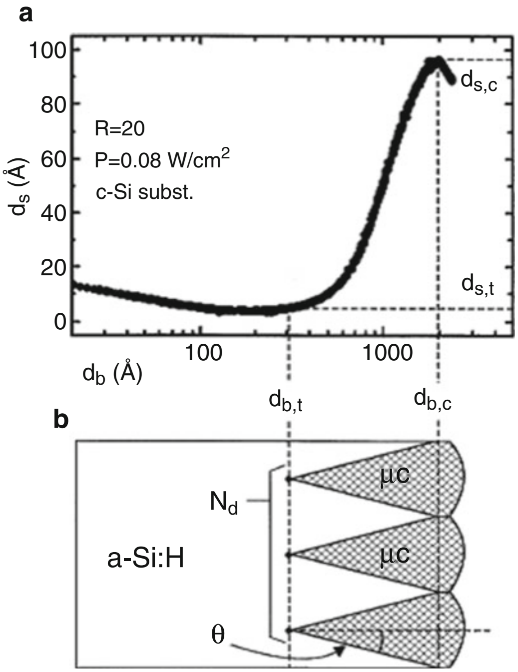

Fig. 18 (**a**) Surface roughness layer thickness (d_s) versus bulk layer thickness (d_b) for the R = 20 Si:H film; (**b**) schematic of the cone growth model used to estimate the crystallite nuclei density and cone angle based on the surface roughness evolution (Collins et al. 2003)

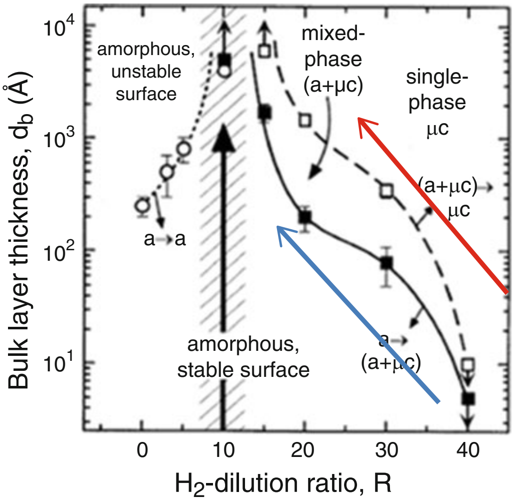

Fig. 19 A phase diagram of Si:H film deposition under a condition given in Collins et al. (2003)

microcrystalline phases and keep it out of the mixed-phase zone; therefore, to make high efficiency a-Si:H solar cells, one should design a process along the blue arrow; similarly, for high efficient μc-Si:H solar cells, they are made with a condition close to the transition from microcrystalline to amorphous phases but still in the microcrystalline phase; therefore, one should design a process along the red arrow in the figure for high efficiency μc-Si:H solar cells.

The crystalline evolution has several negative impacts on the solar cell performance. First, the a-Si:H incubation layer has a high resistivity than μc-Si:H, in which photocarriers have to pass through with a low mobility that results in additional series resistance and reduces the FF. Second the mixed phase region normally has a high defect density that affects the cell performance remarkably, and finally the top layer with very high crystallinity easily forms a high density of microvoids and cracks, which results in the postdeposition impurity diffusion. Therefore, for high efficiency solar cells, one has to avoid the crystalline evolution.

To resolve the crystalline evolution issue, a hydrogen dilution profile technique was proposed by Yan et al. (2004a, b) and was proven to be an effective method to improve the performance of μc-Si:H solar cells. The basic concept of hydrogen dilution profile is consistent with the red arrow as in Fig. 19. A very high hydrogen dilution ratio at the starting of the deposition removes the a-Si:H incubation layer and follows with a continual decrease of hydrogen dilution with deposition time to maintain the same crystallinity as the film growth. Figure 20 shows an cross-sectional TEM image of a μc-Si:H film deposited with a hydrogen dilution profile, where the bottom thin layer is an a-Si:H n-layer. The result shows no a-Si:H incubation layer and a uniform crystalline structure. It demonstrates the effectiveness of the hydrogen dilution profile on the controlling of crystalline evolution. This technique is also effective on the solar cell efficiency improvement. Table 1 lists the current density versus voltage (J-V) characteristics of the μc-Si:H solar cells made with various hydrogen dilution profiles (Yan et al. 2004a, b). Three baseline cells show a J_{sc} around 22–23 mA/cm^2. But the two cells with 20% longer intrinsic layer

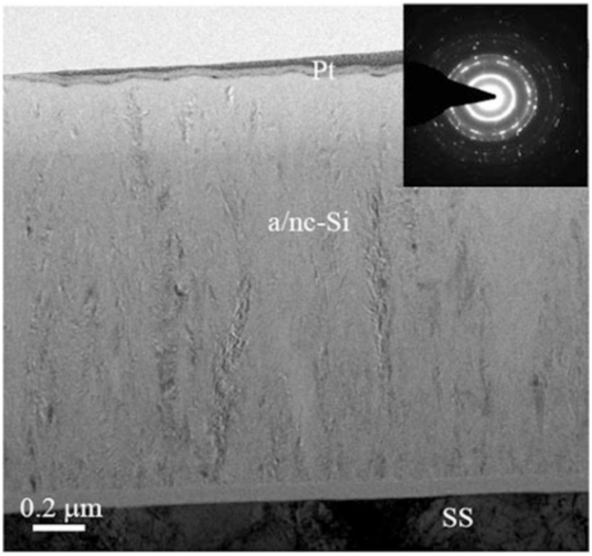

Fig. 20 A cross-sectional TEM image of a μc-Si:H film deposited with a hydrogen dilution profile, showing an uniform crystalline structure

Table 1 Performance parameters of μc-Si:H solar cells made with various hydrogen dilutions

Sample #	J_{sc} (mA/cm^2)	V_{oc} (V)	FF			Eff (%)	Comments
			AM1.5	Blue	Red		
14,554	22.58	0.495	0.603	0.652	0.615	6.74	Flat baseline
14,568	22.15	0.488	0.599	0.648	0.599	6.48	
14,596	22.05	0.482	0.622	0.656	0.605	6.61	
14,559	21.48	0.482	0.632	0.678	0.637	6.54	20% thicker than baseline
14,562	21.57	0.484	0.652	0.692	0.651	6.81	
14,578	23.22	0.482	0.594	0.646	0.631	6.63	Profiling 1
14,580	22.58	0.484	0.644	0.688	0.662	7.04	Profiling 2
14,612	24.41	0.485	0.616	0.659	0.647	7.29	Profiling 3
14,619	24.63	0.492	0.645	0.683	0.641	7.81	Profiling 4
14,642	23.42	0.502	0.681	0.706	0.700	8.01	Profiling 5
14,660	**25.15**	**0.502**	**0.663**	**0.679**	**0.693**	**8.37**	**Profiling 6**

deposition time show a lower J_{sc}, mainly due to the reduction in the long wavelength response. The six hydrogen dilution profiles from 1 to 6 are designed with the increase of the grading slope of the hydrogen dilution ratio but with the same average hydrogen dilution, which means that profile-6 has highest hydrogen dilution ratio at the beginning of the deposition but the lowest at the end of the deposition. It clearly demonstrates that the hydrogen dilution profiling has improved the cell performance significantly, especially the long wavelength response. The cells with the constant hydrogen dilution have an average initial active-area efficiency of 6.6%. By using the hydrogen dilution profiling, an efficiency of 8.37% was obtained. The hydrogen dilution profile technique has been widely used in the community for improving μc-Si:H solar cell performance. Because the μc-Si:H deposition is a multivariable system and the material structure and quality depend on all of the parameters, the crystalline evolution could be also controlled by other parameters such as the excitation power and temperature. Han et al. (2010) using a RF power profile method achieved the same effect as hydrogen dilution profile. We need to point out that the initial grow of the film is very important such that one has to eliminate the a-Si:H incubation layer. Several methods have been proposed for making incubation free μc-Si:H layers such as a very high hydrogen diluted seed layer (Vetterl et al. 2003), a prehydrogen plasma treatment (Zhang et al. 2011), and using reactive etching gases such as F or Cl containing gases (Kasouit et al. 2002; Chung et al. 2011).

Impurity Issue and Controlling

As pointed previously, most of μc-Si:H films made in the early stage showed a high conductivity with N-type carrier transport, and it was found that the high conductivity is caused by O impurity because O becomes weak donors in μc-Si:H. The tolerance for O in a-Si:H is in the order of 1–2 × 10^{19} cm^{-3}, but it is only 5 × 10^{18} cm^{-3} in μc-Si:H (Merdzhanova et al. 2012; Woerdenweber et al. 2012). The incorporation of O in

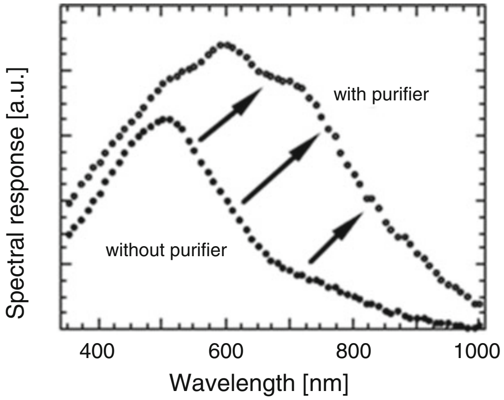

Fig. 21 EQE comparison of μc-Si:H solar cells made with and without a gas purifier in the deposition system (Torres et al. 1996)

μc-Si:H comes from the residual impurities in the deposition system, gases, and postdeposition diffusion from the ambient. In order to reduce the unintentional doping, using a clean system with high purity gases, especially H_2, is critical for the deposition of high quality μc-Si:H films. In addition, optimized deposition conditions are essential for highly compacted material structure to avoid postdeposition impurity diffusion.

Figure 21 shows a comparison of two μc-Si:H silicon solar cells with different impurity levels achieved with and without a gas purifier. It clearly demonstrates that the gas purifier significantly improved the cell performance. Secondary ion mass spectroscopy (SIMS) analysis showed that the gas purifier can reduce the O level from above 10^{19} cm^{-3} down to 5×10^{18} cm^{-3} (Meier et al. 1996).

The impurities in μc-Si:H are not only incorporated in during the deposition, but also diffuse into the materials after the deposition and air exposure if the materials are not compact enough. Small angle X-ray scattering (SAXS) measurements showed that unoptimized μc-Si:H materials could have a few percent of microvoids in volume (Williamson 2003), which allow impurities diffuse into the materials and degrade the solar cell performance. Figure 22 (upper) shows the dark-conductivity of an individual μc-Si:H layer as a function of time keeping the sample in the ambient without light soaking, which clearly shows an increase of the dark-conductivity and associates with the reduction of activation energy from 0.52 eV to 0.17 eV; while as shown in lower panel of Fig. 22, the μc-Si:H *p-i-n* solar efficiency did not change at all during the air exposure, which was explained with the blocking the impurity diffusion by the back ZnO/metal contact in the solar cell (Meier et al. 1998).

The *n-i-p* μc-Si:H solar cells are not as lucky as the *p-i-n* solar cells because the *n-i-p* solar cells are normally deposited on nontransparent substrates and the top contact on the *p*-layer is an Indium-Tin-Oxide (ITO) layer with a thickness of ~75 nm for the antireflection effect, which is not effective to block the impurity diffusion. Figure 23 shows the J-V characteristics and external quantum efficiency (EQE) curves of an early unoptimized μc-Si:H *n-i-p* solar cell in the as-deposited state and after 30 days keeping in the ambient (Yan et al. 2002). One can clearly see that the solar cell performance was degraded just keeping the cell in the ambient. A controlled experiment showed that the

Fig. 22 Comparison of an intrinsic μc-Si:H film and the corresponding *p-i-n* solar cell as the function of air exposure after deposition. The film was characterized by the dark conductivity measurement and the cell by J-V measurements under AM 1.5. The dashed lines are drawn to guide the eye (Meier et al. 1998)

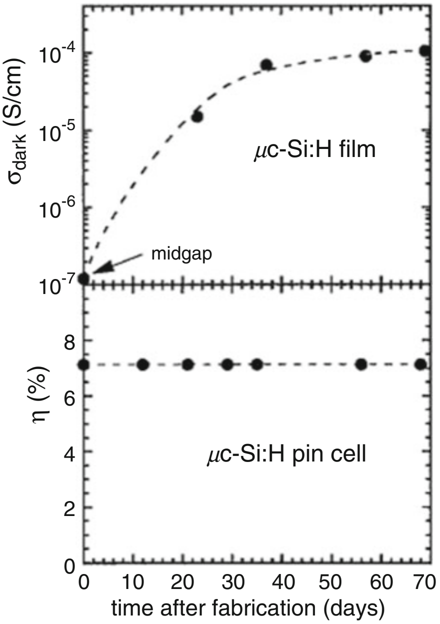

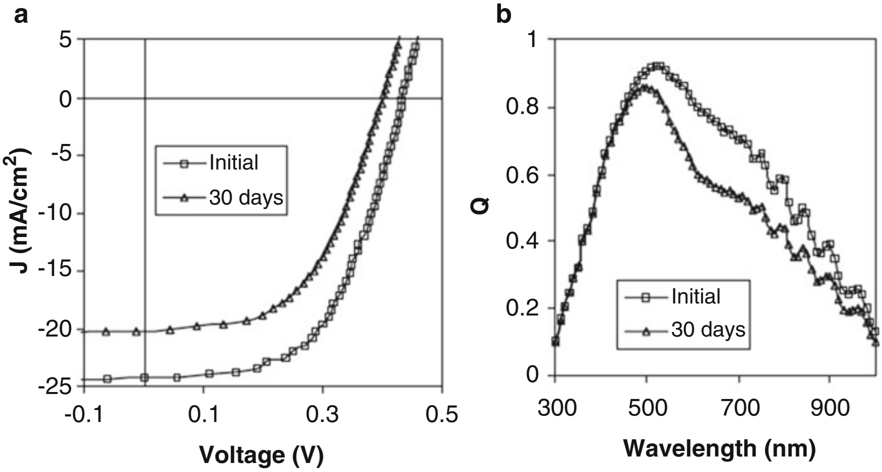

Fig. 23 J-V characteristics and quantum efficiency (Q) of a μc-Si:H solar cell in the initial state and after 30 days exposure in the ambient without light soaking (Yan et al. 2002)

ambient degradation results mainly from the moisture in the air because keeping the cells in N_2 and dry cold air prevented the ambient degradation, but the cell in hot and humid air accelerated the degradation (Yan et al. 2002). The ambient degradation mainly happened in the early stage of μc-Si:H solar cell study. After the

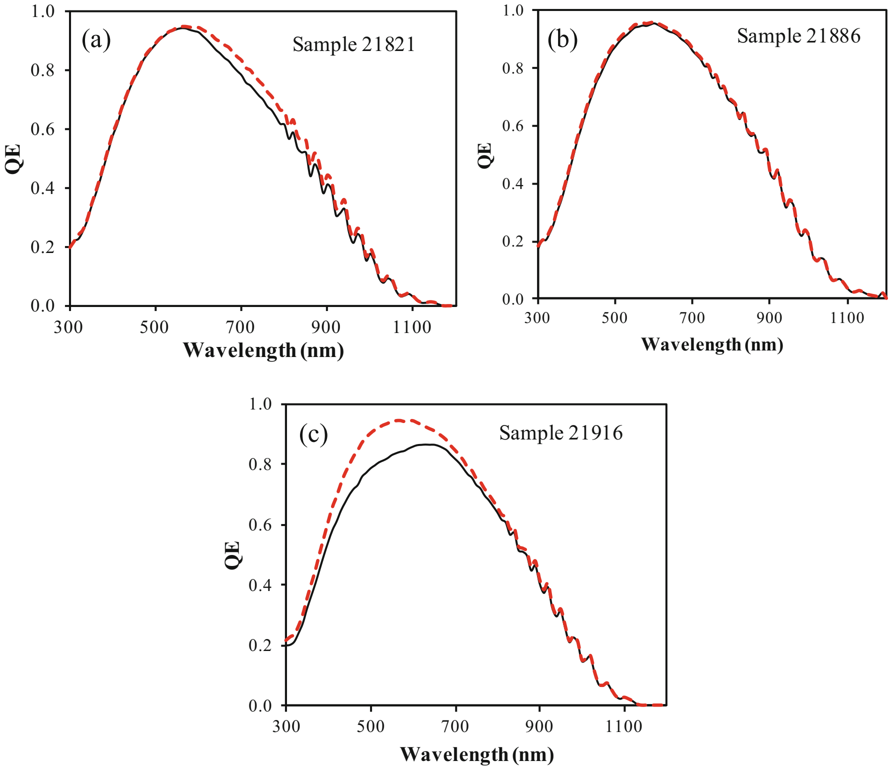

Fig. 24 Quantum efficiency (QE) measured under -5 V bias (red dash lines) and the short circuit condition (thin solid black lines) for three samples with different QE losses, where (**a**) Sample 21,821 has a long wavelength QE loss; (**b**) Sample 21,886 has a minimal QE loss; and (**c**) Sample 21,916 has a short wavelength QE loss (Yue et al. 2012b)

optimization of the deposition process, high quality μc-Si:H materials and *n-i-p* solar cells with compact structures and low density of microvoids do not surfer the ambient degradation problem. The optimization of the deposition process will be addressed later.

For the high quality μc-Si:H materials and high efficiency μc-Si:H solar cells, the impurity is still an issue. Yue et al. (2012a, b) have carefully studied the effect of impurity on high efficiency μc-Si:H solar cells. Because of the high sensitivity of μc-Si:H to impurity, most high efficiency solar cells are deposited in multichamber systems to reduce the cross-contaminations. Even in multichamber systems, the cross-contaminations cannot be absolutely avoided. Especially for B contamination, the level of 10^{16} cm^{-3} of B can cause a noticeable effect on μc-Si:H solar cell performance. An example is given in Fig. 24, where the quantum efficiencies (QE) of three μc-Si:H solar cells with the same back ground B contamination at 2×10^{16} cm^{-3}, but with different O concentrations obtained by different deposition chamber conditionings as shown in Fig. 25. The QE measurements were made under

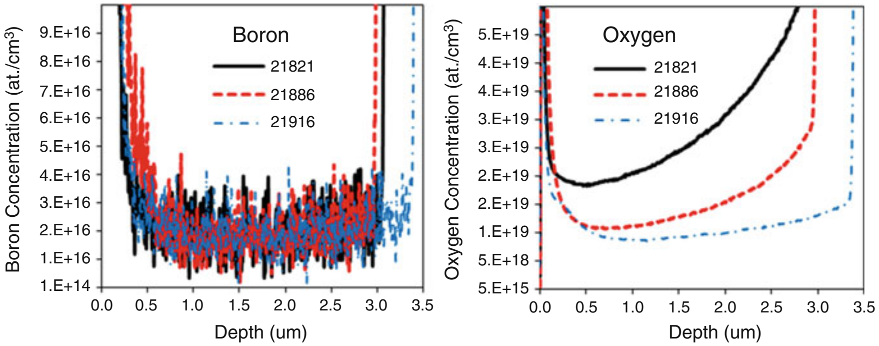

Fig. 25 Boron and oxygen profiles measured with SIMS in three μc-Si:H solar cells made with different chamber conditionings (Yue et al. 2012b)

zero bias (short circuit) and −5 V bias conditions. The photocurrent difference obtained from the two curves is called QE loss, which reflects the recombination loss. Because a revise bias enhances the electric field in the intrinsic layer and reduces the recombination rate, the larger the difference between the reverse biased QE and the zero biased QE, the more the recombination loss is. In addition, the recombination occurring in different regions in the intrinsic layer reflects in the different wavelength ranges in the QE spectrum. A short wavelength light is mainly absorbed in the shallow region near the *p/i* interface; thus, the short wavelength QE loss reflects the recombination occurs mainly in the region near the *p/i* interface, while a long wavelength light is absorbed uniformly in the entire intrinsic layer, but the holes generated in the region near the *i/n* interface travel a longer distance than those generated in the *p/i* region; thus, the long wavelength loss detects the recombination in the region near the *i/n* interface. If the solar cell has more effective P-type contamination than effective N-type contamination, the electric field in the *p/i* region is weakened and in the *i/n* region is enhanced. As a result, a noticeable short wavelength loss is observed, while for the same reason a long wavelength QE loss measures an N-type contamination. Comparing the results in Figs. 24 and 25, one can see the correlation between the QE losses and the impurity distributions. Sample 21,821 has a high O content, especially in the *i/n* region, and has a noticeable long wavelength QE loss; sample 21,886 has the medium O content, the QE loss is almost undetectable, which means that the P-type and N-type contaminations are compensated each other, while sample 21,916 has the lowest O content, which shows a large short wavelength QE loss because the O contamination is not enough to compensate the B contamination. Table 2 lists the performance parameters of these three solar cells. Although sample 21,916 has the lowest O contamination, it has the lowest performance because of the loss of photo-current in the short wavelength; the middle O contaminated cell has the best efficiency of 10.5% with less than 1% of QE loss; but when the high O content is more than enough to compensate the B contamination as in 21,821, it causes the long wave length QE loss. From these results, one can see how sensitive the μc-Si:H solar cells to impurities.

Table 2 The performance parameters of μc-Si:H solar cells with different impurity contaminations (Yue et al. 2012b)

Sample	Source	V_{oc} (V)	FF	QE(mA/cm^2) 0 V	QE(mA/cm^2) -5 V	QE loss (%)	Eff. (%)
21,821 (N-type)	Filter 610	0.525	0.720	15.15	16.15	6.19	5.73
	AM1.5	0.541	0.720	26.54	27.65	4.01	10.34
21,886 (comp)	Filter 610	0.529	0.709	16.93	17.07	0.82	6.35
	AM1.5	0.543	0.691	28.15	28.43	0.98	10.56
21,916 (P-type)	Filter 610	0.516	0.649	15.79	16.34	3.37	5.29
	AM1.5	0.532	0.630	26.02	27.90	6.74	8.72

The above results demonstrate that the μc-Si:H solar cells are very sensitive to impurities. For the P-type contamination by B, a very low level at 10^{16} cm^{-3} could cause a noticeable change in the cell performance as indicated by the short wavelength loss. The reason for such a low tolerance is that B is a strong donor in μc-Si:H. In the early study, Meier et al. (1996) first used B to compensate the unintentional O doing to improve μc-Si:H solar cell performance and achieved reasonable good results at the time and named the technique as microdoping. However, the high sensitivity of B doing leads to a narrow window for a proper compensation that also depends on the back ground N-type contamination; therefore, the microdoping technique might be only used as a method to study the fundamental contaminations and prove some concepts, but hardly be used in real high efficiency solar panel production. Similar to B, the sensitivity of μc-Si:H to P is also very high. However, the back ground contaminations from O and N cover the residual P effect in most cases, and less attention has been made on P contamination. From the real solar cell fabrication point of view, multichamber systems with a very low degassing rate and using high pure gases are preferred. In addition, special cares must be taken in the process to avoid any cross contaminations from the doing gases.

Light-Induced Metastability in μc-Si:H Solar Cells

One of the advantages of μc-Si:H solar cells over a-Si:H counterparts is low or no light-induced degradation. Early studies showed that μc-Si:H solar cells did not show any light-induced degradation as proven by Fig. 26 (Meier et al. 1998), where the μc-Si:H solar cell efficiency did not change after 1000 hours of light soaking, while the a-Si:H solar cell degraded by almost 50%. However, some μc-Si:H solar cells also show some degrees of light-induced degradations, especially those with a high percentage of amorphous phase.

Yan et al. (2004c) did a systematic study on the light-induced degradations in μc-Si:H solar cells and compared a-Si:H and a-SiGe:H solar cells by using different light sources to determine where the light-induced degradation occurs. The design of the experiment is based on the hypothesis below. High efficiency μc-Si:H solar cells are usually deposited near the transition from the microcrystalline to the amorphous

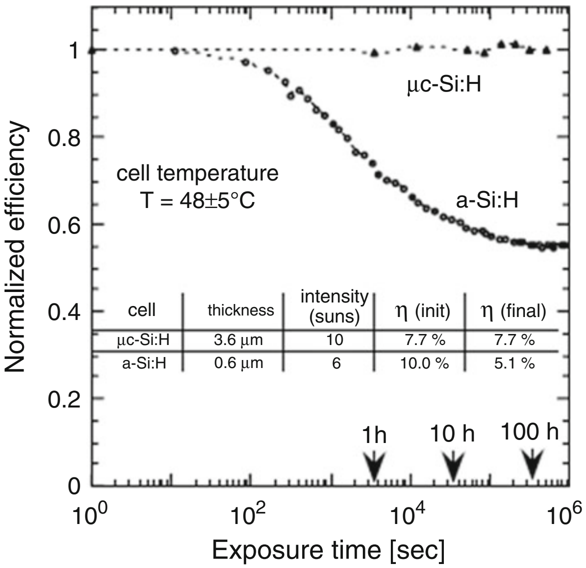

cell	thickness	intensity (suns)	η (init)	η (final)
μc-Si:H	3.6 μm	10	7.7 %	7.7 %
a-Si:H	0.6 μm	6	10.0 %	5.1 %

Fig. 26 Comparative behavior of a μc-Si:H solar cell and an a-Si:H solar cell under intensive light illumination, from a sodium lamp. Efficiencies were measured before/after light soaking under standard conditions (Meier et al. 1998)

phase (Vetterl et al. 2000; Roschek et al. 2000), which means that a finite amount of the amorphous phase still exists in the μc-Si:H materials used in high efficiency solar cells. One therefore suspects that some light-induced degradations may present in the μc-Si:H solar cells due to the amorphous component. Indeed, Klein et al. (2003) found that μc-Si:H solar cells made with hydrogen dilution close to the microcrystalline/amorphous transition showed light-induced degradations and that the degree of degradations depended on the dilution ratio and hence on the crystalline volume fraction. In general, μc-Si:H can be considered as a two-phase material with crystalline grains surrounded by amorphous tissues. The photons with energy higher than the bandgap of a-Si:H are mainly absorbed in the amorphous phase while the lower energy ones in the grains. Inside the grains, the material properties are similar to crystalline silicon, and no light-induced defect generation is expected. Therefore, one may speculate that no light-induced defects are generated in grains when exposed to red light with photon energies lower than the optical band gap of a-Si:H. If this hypothesis is true, then one expects very little or no light-induced degradation in the μc-Si:H bottom cell of an a-Si:H/μc-Si:H double-junction or of an a-Si:H/a-SiGe:H/μc-Si:H triple-junction structure because the high energy photons are absorbed in the a-Si:H top and a-SiGe:H middle cells and do not reach the μc-Si:H bottom cell.

To prove or disprove the above hypothesis, a light soaking experiment was made on μc-Si:H and a-SiGe:H solar cells under different light spectra. Figure 27 shows a comparison of the normalized maximum power, P_{max}, as a function of light soaking time for a μc-Si:H solar cell and an a-SiGe:H solar cell, where the red and blue lights were obtained using a 665 nm long-pass filter and a 650 nm short-pass filter, respectively. The long-pass filter allows photons with energies lower than 1.86 eV

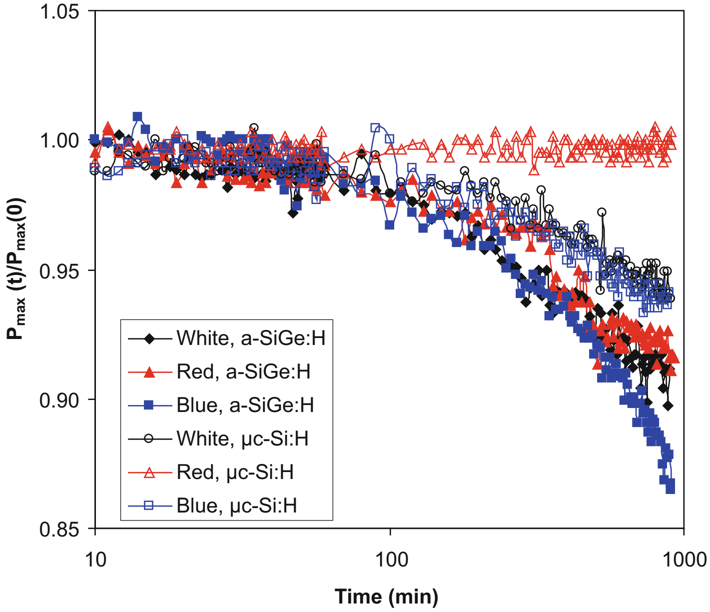

Fig. 27 Light soaking kinetics of the normalized efficiency of a μc-Si:H single-junction solar cell and an a-SiGe:H single-junction solar cell with different spectral regions

Table 3 Summary of light soaking results for μc-Si:H single-junction solar cells. IN represents the initial state, LS the light soaked state, and DEG the percentage of degradation

Light	State	J_{sc} (mA/cm^2)	V_{oc} (V)	FF	Eff. (%)
White	IN	22.20	0.474	0.621	6.53
	LS	22.00	0.467	0.598	6.14
	DEG.	0.9%	1.48%	3.70%	5.97%
Red	IN	22.19	0.472	0.620	6.49
	LS	22.11	0.473	0.619	6.47
	DEG	0.36%	0%	0%	0.31%
Blue	IN	21.98	0.476	0.621	6.50
	LS	21.78	0.469	0.591	6.04
	DEG	0.91%	1.47%	4.83%	7.08%

to pass through to illuminate the sample. For the μc-Si:H cell, the light intensities for the two spectra were adjusted to generate J_{sc}~44 mA/cm^2, which is approximately twice of the J_{sc} under AM1.5 illumination. For the a-SiGe:H cell, the light intensities were adjusted to generate J_{sc}~46 mA/cm^2 with the same consideration. Tables 3 and 4 summarize the J-V characteristics of the two series of cells in their initial and light soaked states. We need to point out that the light-soaked state is not a saturated state since only 15 hours of light soaking were made. Figure 27 clearly shows that there is no light-induced degradation for the μc-Si:H cell under the red light, but

Table 4 Summary of light soaking results for a-SiGe:H single junction solar cells

Light	State	J_{sc} (mA/cm^2)	V_{oc} (V)	FF	Eff (%)
White	IN	23.10	0.628	0.601	8.72
	LS	22.88	0.601	0.567	7.80
	DEG	0.95%	4.30%	5.66%	10.55%
Red	IN	23.91	0.614	0.587	8.62
	LS	23.48	0.601	0.563	7.94
	DEG	1.80%	2.12%	4.09%	7.89%
Blue	IN	23.50	0.621	0.572	8.35
	LS	22.91	0.591	0.539	7.30
	DEG	2.51%	4.83%	5.77%	12.57%

some degradations under the white light (see Table 3) and more degradation under the blue light. As explained above, the absence of light-induced degradation under the red light illumination is due to the lack of absorption in the amorphous phase and no light-induced defect generation in the crystalline phase. In contrast to the red light illumination, the white and blue light illuminations showed noticeable degradation in the cell performance. The difference in the degradation between the white- and blue-light soaked μc-Si:H cells could be explained in two ways. First, the blue light has a large portion of photons absorbed in the amorphous phase, which produces defects. Second, the blue light is absorbed near the *i/p* interface more than in the bulk. Pawlikiewicz and Guha (1988) showed that the *i/p* junction is the dominant junction and any change in this junction causes noticeable changes on the cell performance. For the a-SiGe:H cell, we consider the material to be homogenous having one optical band gap of about 1.5 eV. The differences among the light soaking results with the three lights with different spectra are mainly due to the second mechanism discussed above. Overall, the light-induced degradation in μc-Si:H is much less than that in the a-SiGe:H cell even under white and blue light.

As pointed out earlier, the spectrum dependence of light-induced degradation in μc-Si:H solar cells has a significant impact on the real solar module application. Thin film silicon solar modules are normally made with a-Si:H/μc-Si:H double-junction, a-Si:H/a-SiGe:H/μc-Si:H triple-junction, and a-Si:H/μc-Si:H/μc-Si:H triple-junction cell structures. The μc-Si:H middle and bottom cells do not see the blue light and therefore do not surfer any light-induced degradation, and overall multijunction solar cell stability is significantly improved. Yue et al. demonstrated that high efficiency a-Si:H/μc-Si:H/μc-Si:H solar cells degraded only 3–5% after prolonged light soaking and a stable cell efficiency of 13.6% was achieved with this cell structure (Yue et al. 2006b).

In a-Si:H solar cells, the metastability was also observed under a forward bias (Street 1991). The physics is similar to the Staebler-Wronski effect under light soaking. Under a forward bias, electrons and holes are injected from the *n* side and *p* side into the *i*-layer, respectively, and recombine there. The electron-hole recombination releases energy, generates metastable defects in the *i*-layer, and hence degrades the cell performance. A question is whether or not a forward bias carrier

Fig. 28 The kinetic changes or normalized FF under 1 V forward bias for the a-Si:H, a-SiGe:H, and μc-Si:H solar cells (Yue et al. 2007)

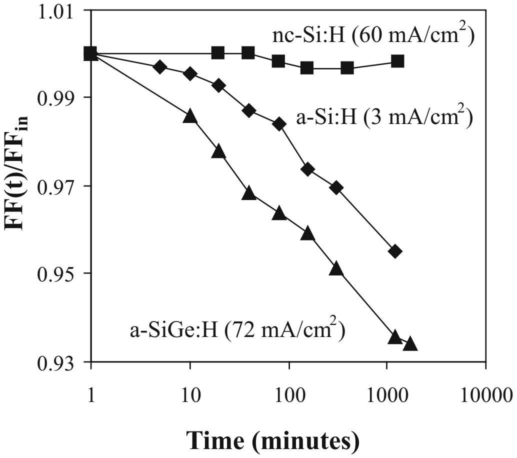

injection results in any degradation in μc-Si:H solar cell. Because the carrier transport mainly takes place in the crystalline phase and the recombination would take place there as well. As shown by the red light soaking experiment, the recombination in the grains does not produce any degradation in μc-Si:H solar cell; therefore, one would expect that a forward bias on μc-Si:H should not result in any degradation in the cell performance.

Figure 28 shows a comparison of forward injection current-induced FF changes as a function of forward bias time (Yue et al. 2007). Three solar cells of a-Si:H, a-SiGe:H, and μc-Si:H were under forward bias of 1 V, which leads to the initial forward current densities of 3 mA/cm^2 for the a-Si:H cell, 72 mA/cm^2 for the a-SiGe:H cell, and 60 mA/cm^2 for the nc-Si:H cell. The FF of the a-SiGe:H degrades significantly; the a-Si:H cell also shows some degrees of degradation even though the forward current density is only 3 mA/cm^2, while the μc-Si:H cell does not degrade within the experimental errors. This experiment proved that the recombination in the crystalline phase indeed does not produce metastable defects to degrade the μc-Si:H solar cell performance.

Another interesting phenomenon of light-induced metastability in μc-Si:H is the electric bias effect (Yue et al. 2005, 2006b, 2007). For a-Si:H solar cells, it has been found that a reverse bias on an a-Si:H solar cell reduces the magnitude of the light-induced degradation because the reverse bias enhances the electric field in the intrinsic layer and reduces the probability of recombination, which is the driving force of the Staebler-Wronski effect (Yang et al. 1992; Yang et al. 2002). However, an electric bias on μc-Si:H solar cells has an opposite effect on the light-induced degradation. A negative bias enhances the light-induced degradation, but a forward bias reduces the light-induced degradation as shown in Fig. 29 (Yue et al. 2005, 2007), where the light-induced degradation of FF under an AM1.5 illumination is plotted as a function of applied bias. In this experiment, eight μc-Si:H cells on the same substrate were light-soaked

Fig. 29 Light-induced degradation in FF versus the electrical bias during light soaking, where ΔFF denotes the variations in FF. The light soaking was carried out at 50 °C under one sun white light for 309 h

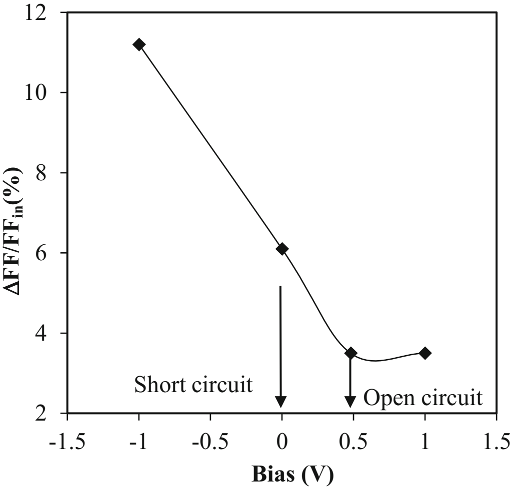

simultaneously under 100 mW/cm^2 white light at 50 °C with various bias conditions of -1 V, short circuit (0 V), open circuit (+0.48 V), and +1 V. To check the reproducibility of the degradation rate, two cells at each bias condition were included. The short circuit corresponds to the 0 V bias, and the open circuit is considered to be a forward bias of V_{oc}, which is around 0.48 V. It is clearly seen that the light-induced degradation in FF was increased by the increase of the magnitude of the reverse bias. Under the -1 V bias condition, the FF degrades on the average by 10.9%, while the FF degrades only by 7.6% under the short circuit condition. Under the open circuit and +1 V bias conditions, however, the degradation in the FF is the same, around 3.8%. This unusual phenomenon has been repeatedly observed and confirmed as the universal characteristics of μc-Si:H solar cells. To explain the observation, Yue et al. proposed a “back-to-back” diode module. For details, please refer Yue et al. (2005, 2006a, 2007).

To summarize the metastability of μc-Si:H solar cells, we make the following conclusions. First, the light-induced degradation in μc-Si:H solar cells is generally lower than in a-Si:H solar cells and some μc-Si:H solar cells even show no light-induced degradation. Second, the light-induced degradation depends on the crystallinity in the intrinsic layer; the high the crystallinity, the lower the light-induced degradation is. Third, the light-induced degradation is only caused by the photons with the energy higher than the bandgap of a-Si:H phase, and no light-induced degradation results from red light illumination, which indicates that the light-induced degradation occurs only in the amorphous phase and grain boundaries. Fourth, a double-carrier injection by a forward electric bias does not cause any degradation in μc-Si:H solar cells, which is different from a-Si:H solar cells. Finally, during light soaking, a revisers electric bias enhances the light-induced degradation and a forward bias reduces the light-induced degradation, which is also opposite with a-Si:H solar cells. Among these characteristics, the most important feature is no light-induced degradation with red light because μc-Si:H solar cells are normally used as the middle and bottom cells in multijunction solar cells, where the high energy photons are absorbed by the a-Si:H top cell.

Light Trapping in μc-Si:H Solar Cells

Although μc-Si:H has a much broader absorption spectrum than a-Si:H, which covers up to 1100 nm, the absorption coefficients are still low in the long wavelength region because of the indirect band gap absorption. Therefore, the required μc-Si:H thickness for effectively absorbing the sun light is much thicker than a-Si:H. However, even the carrier mobility in μc-Si:H is higher than in a-Si:H, the absorber layer in μc-Si:H solar cells still cannot increase too much without significantly suffering the loss in FF and V_{oc}. Considering all of the performance parameters, the optimized μc-Si:H intrinsic layer thickness has been determined to be in the range of 3–5 μm. However, with the consideration of production efficiency and current mismatching, the μc-Si:H intrinsic layer could be limited to 1–2 μm for double-junction cells and 3–5 μm for triple-junction solar cells, which is still not thick enough to absorb the sun light to give enough current. Therefore, effective light trapping techniques are needed. Based on the solar cell structures, the light trapping methods for *p-i-n* and *n-i-p* structured μc-Si:H solar cells are different.

The light trapping in *n-i-p* structured solar cells is mainly from the scattering at the back interface between the silicon layer and the back reflector (BR). The top TCO is ~75-nm thick highly conductive ITO, which cannot provide enough textures for light trapping. The thin ITO functions as an antireflection (AR) coating to reduce the reflection loss. The BRs are made with Ag/ZnO or Al/ZnO double-layer structures as shown in Fig. 30. Figure 31 shows a comparison of EQE curves of three μc-Si:H solar cells deposited with the same recipe but on different substrates, where a significant enhancement of the long wavelength response is achieved by the light trapping. The μc-Si:H solar cell on the bare stainless steel has a total photocurrent density of 15.56 mA/cm^2; the ones on the Al/ZnO and Ag/ZnO BRs have the values of 20.48 mA/cm^2 and 24.48 mA/cm^2 and the gains of 31.6% and 57.3%,

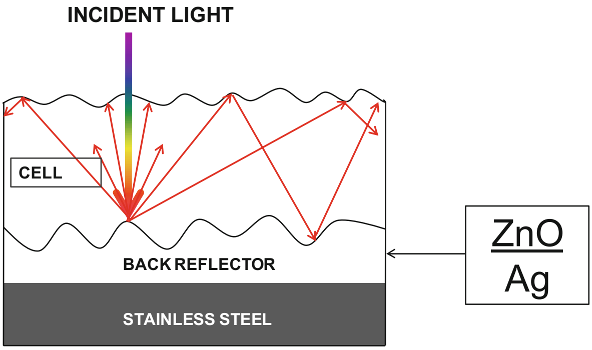

Fig. 30 Schematic of light trapping in an *n-i-p* structured μc-Si:H solar cell by a ZnO/Ag back reflector

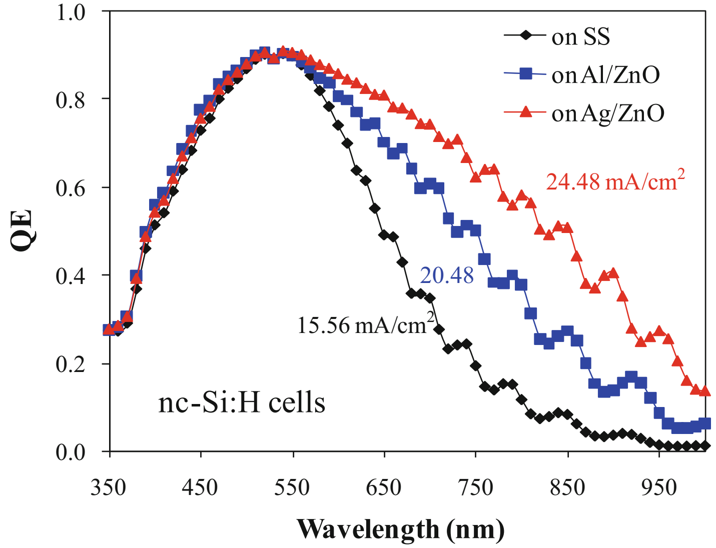

Fig. 31 EQE curves of three μc-Si:H solar cells deposited with the same recipe but on different substrates

respectively. It demonstrates that the Al/ZnO and Ag/ZnO are very effective for light trapping in μc-Si:H solar cells.

The design and optimization of BR should take the following considerations. The textured metal layer (Ag or Al) reflects and scatters the light that reaches the BR; the ZnO layer reduces the plasmonic losses at the Ag/Si interface by shifting the plasmonic resonance frequency to the short wavelength region where the light is absorbed in the first path. The ZnO layer also adds additional textures for light scattering. Therefore, the effectiveness of light trapping is determined by three factors of (1) the reflectivity, (2) the scattering, and (3) the reduction of surface absorption. For high efficiency μc-Si:H solar cells, Ag is normally used in the BR for its high reflectivity as shown in Fig. 30, but Al is used in some products for low cost. The scattering could occur at the texture surface of Ag and the texture surface of ZnO. The scattering at the Ag surface is much more effective than at ZnO surface, which means that a small scale texture on the Ag surface could provide a high level of scattering, while the texture of Ag surface could cause the plasmonic absorption. Thus, in order to reduce the plasmonic absorption, a flat Ag surface and a highly textured ZnO layer are preferred theoretically, and it has been also confirmed in a-SiGe:H solar cells. However, a high textured ZnO could cause the degradation of μc-Si:H quality as discussed later. Therefore, the design and optimization of Ag/ZnO BR need to compromise the textures of ZnO and Ag. Experimentally, it was found that a textured Ag with a thin ZnO (100 nm) is a good choice of the ZnO/Ag BR for μc-Si:H solar cells (Yan et al. 2012; Sivec et al. 2012). The texture on the Ag surface is much more effective than on ZnO to scatter light and therefore some moderate

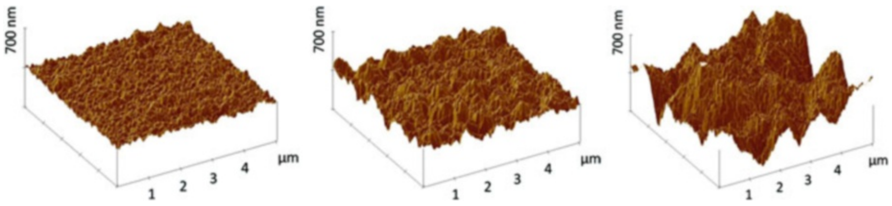

Fig. 32 AFM images of three Ag/ZnO BRs with different Ag textures, (left) low texture with RMS = 17 nm, (middle) medium texture with RMS = 40 nm, and (right) high texture with RMS = 118 nm

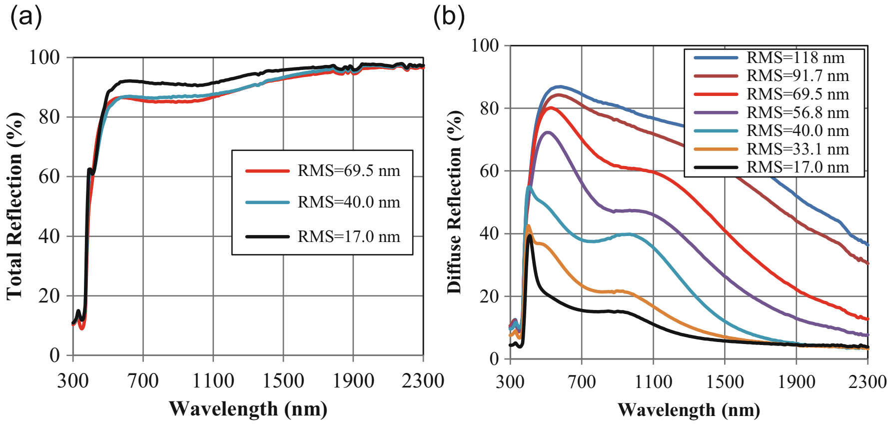

Fig. 33 The (**a**) total and (**b**) diffusive reflection spectra of Ag/ZnO back reflectors with various textures as measured by the RMS from AFM images

textures are good enough to provide the scattering for good light trapping. On the other hand, the thin ZnO layer shifts the plasmonic resonance frequency to the short wavelength region, where the light is absorbed before reaching the back contact. Figure 32 shows the surface morphologies of three ZnO/Ag BRs, where the textures are mainly from the Ag layer and the ZnO layers are the same for all of the samples with a thickness of 100 nm. Figure 33 plots the total and diffuse reflection spectra of the BRs. It shows that the total reflectance spectrum decreases slightly with the increases of Ag texture, which could result from the absorption at the Ag/ZnO interface and the light trapping in the ZnO layer because the optical constant of ZnO is larger than in air. However, the diffusive reflectance spectra are very different with different Ag texture. A significance increase in the diffusive reflectance is observed by the increase of Ag texture, implying a potential enhancement for light trapping.

The same μc-Si:H solar cells with 1 μm thick μc-Si:H intrinsic layer were deposited on this type of ZnO/Ag BR coated stainless steel substrates with different textures from the Ag layers. The EQE curves of four selected μc-Si:H solar cells are plotted in Fig. 34 and the cell performance parameters are listed in Table 5. It notes

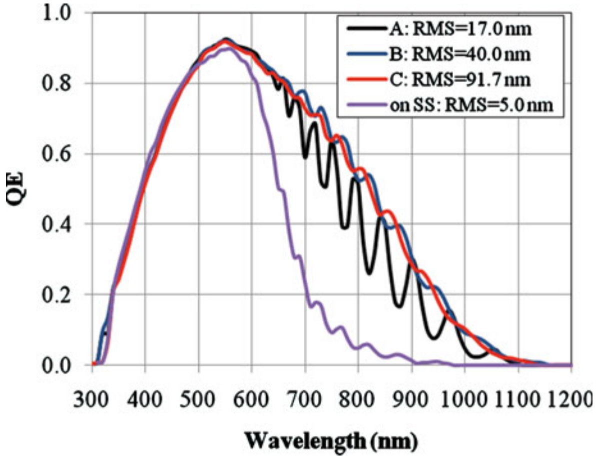

Fig. 34 EQE spectra of μc-Si:H solar cells made with the same recipes but on different Ag/ZnO BRs. The μc-Si:H intrinsic layer is 1 μm

that the solar cells on the Ag/ZnO BR have a significant higher response in the long wavelength region than on the bare SS and demonstrates again the effectiveness of the light trapping. The solar cell on the BR with RMS = 17 nm shows a significant interference fringes, indicating a large amount of direct reflection, while with the increase of the texture, the interference fringes are reduced, associating the enhancement of scattering. The solar cell on the SS has only 15.12 mA/cm^2 of J_{sc}, while the one on the Ag/ZnO BR with RMS = 40 nm has 25.03 mA/cm^2, and a gain of 66% is observed. It is also found that increasing the texture further does not increase the spectral response further even the diffusive reflection is enhanced. Instead, the photocurrent density decreases slightly. Furthermore, the FF also decreases and the EQE loss (ΔQE) increases with the increase of the substrate texture, a phenomenon is often observed in μc-Si:H solar cells, and it relates to the structural defect formation caused by the high textured substrates. The details will be discussed later. By making a thicker μc-Si:H solar cell (3.1 μm) on the optimized Ag/ZnO BR, a high photocurrent density of 30.5 mA/cm^2 was obtained with the J-V curve and EQE spectrum plotted in Fig. 35.

From the above results, we conclude that the optimized Ag/ZnO BRs are very effective to increase the spectral response of μc-Si:H solar cells. A current gain over 60% compared to μc-Si:H solar cells on bare flat SS substrates can be obtained. The best Ag/ZnO BRs with a textured Ag layer and thin ZnO (100 nm) is made with a proper texture of RMS around 40 nm. For the RMS beyond this value, no additional again in the photo-response is observed. Furthermore, the FF of the solar cells decreases with the increase of the surface roughness. With the optimized Ag/ZnO, a short circuit current density more than 30 mA/cm^2 has been obtained with the cell thickness of 3 μm.

The *p-i-n* structures are normally deposited on transparent conducive oxide (TCO) coated glass substrates. Because the light actually illuminates the solar cells on the substrate side and passes through the glass/TCO to reach the semiconductor layers, the substrate is also called "superstrate." The light trapping in the *p-i-n*

Table 5 The J-V characteristics of μc-Si:H solar cells made with the same recipes but on different Ag/ZnO BRs. The μc-Si:H intrinsic layer is 1 μm

RMS (nm)	light	V_{oc} (V)	FF	FF_b	FF_r	QE(0 V) (mA/cm^2)	QE(-3 V) (mA/cm^2)	P_{max} (mW/cm^2)	ΔQE (%)
A	Color			0.722	0.720				
17.0	> 610 nm	0.515	0.738			11.61	11.69	4.41	0.7
	AM1.5	0.530	0.723			22.43	22.55	8.59	0.5
B	Color			0.716	0.72				
40.0	>610 nm	0.522	0.726			13.86	14.16	5.25	2.1
	AM1.5	0.541	0.711			24.62	25.03	9.47	1.6
C	Color			0.703	0.704				
91.7	> 610 nm	0.519	0.717			13.59	14.06	5.06	3.3
	AM1.5	0.537	0.702			24.30	24.98	9.16	2.7

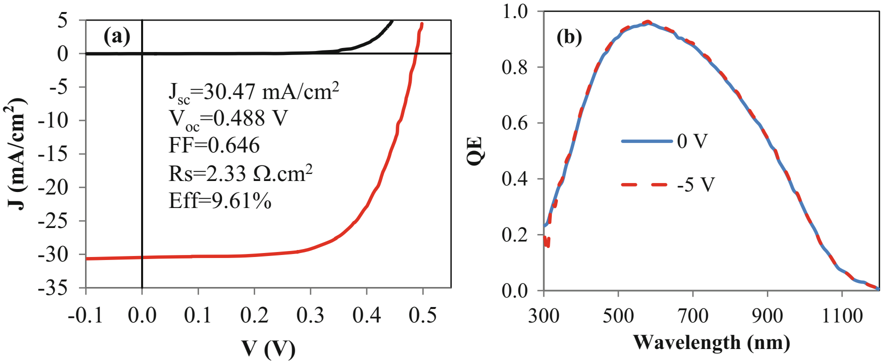

Fig. 35 J-V characteristics and EQE spectrum a μc-Si:H solar cell with total photocurrent density > 30 mA/cm^2

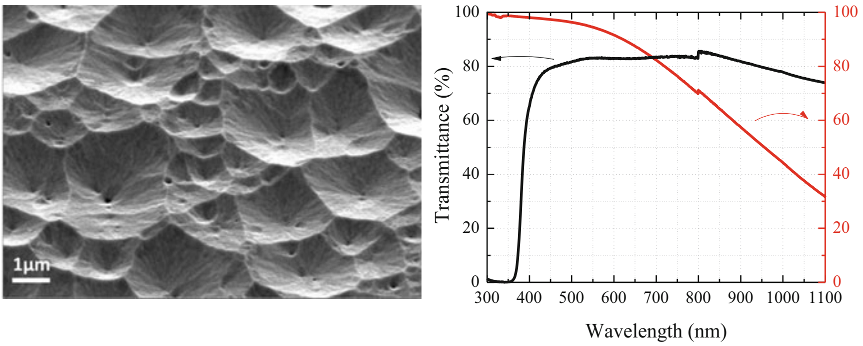

Fig. 36 Tilt-view scanning electron microscope (SEM) images and experimentally measured total transmittance and haze spectra of a magnetron-sputtered and texture-etched AZO

structured solar cells are normally achieved by using a textured TCO layer. Tin Oxide (SnO_2) TCO layer is widely used in a-Si:H alloy based solar cells, but it is not suitable for μc-Si:H solar cell deposition because SnO_2 reacts with the high density atomic hydrogen during the μc-Si:H deposition. Alternatively, ZnO is used as the TCO for μc-Si:H solar cells. Although undoped ZnO already has an N-type transport, the conductivity is not high enough to meet the low series resistance requirement; Al, B, or Ga is added as the doping elements during the ZnO deposition to increase the conductivity. The Al doped ZnO is called AZO, which usually deposited using megaton sputtering of an Al_2O_3 doped ZnO ceramic target. The effectiveness of light trapping strongly depends on the texture of the TCO. Normally, the as-deposited AZO is relatively flat and does not have the required textures for effective light trapping; a chemical etching method using diluted HCl is used to increase the texture of AZO (MuKller et al. 2001; Müller et al. 2003; Hüpkes et al. 2012). Figure 36 shows the surface morphologies of a AZO sample after chemical

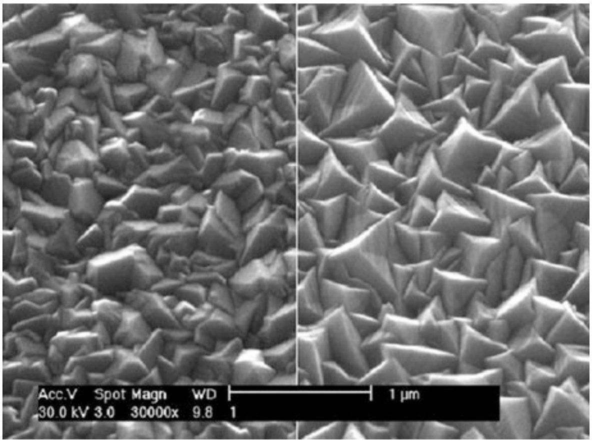

Fig. 37 Comparison of (left) SnO_2 and (right) LP-CVB BZO surface morphology SEM images (Meier et al. 2002)

etching and its transmittance as well as the haze spectra. One can see that the surface texture with "crater-like" structures and the haze is very high in the wide spectrum range.

The surface of sputtered AZO can also be changed by optimizing the deposition process, such as the substrate temperature, film thickness, excitation power, and pressure. Huang et al. (2012) found that adding H_2 during the sputtering process can increase the surface texture. The AZO substrate made with this method shows an effective enhancement for photocurrent in μc-Si:H solar cells. Most importantly, this method can eliminate the chemical etching process and reduce the thin film solar panel manufacturing cost.

The B doped ZnO is called BZO, which is normally made using a low pressure chemical vapor deposition (LP-CVD) process. The textures of the LP-CVD deposited BZO form during the deposition and can be modified by the process parameters, especially the substrate temperature and process pressure (Meier et al. 2002; Nicolay et al. 2011). Figure 37 shows the surface morphology comparison of an LP-CVD prepared BZO sample with the industrially used SnO_2 TCO samples; both samples show very similar surface structures. The LP-CVD deposited BZO has "crystal-like" surface structures instead of the "crater-like" structures on the chemically etched AZO substrates. The LP-CVD deposited BZO is also an effective light trapping substrate for μc-Si:H solar cells and has been incorporated in TEL Solar's thin film silicon solar module manufacturing lines (Cashmore et al. 2016).

As previously mentioned, a highly textured substrate could cause the degradation of μc-Si:H material quality and solar cell performance. If only considering the optical properties for light trapping, a highly textured substrate would be preferred for μc-Si:H solar cells; however, in reality it is much complicated in μc-Si:H solar cell fabrications. The main issue is that the surface texture directly impacts the growth of μc-Si:H materials. It has been found that the crystallites have the tendency to form columnar structures perpendicular to the local growth surface. The shape of the textured surface, such as the average slope and the angle at the bottom of valleys,

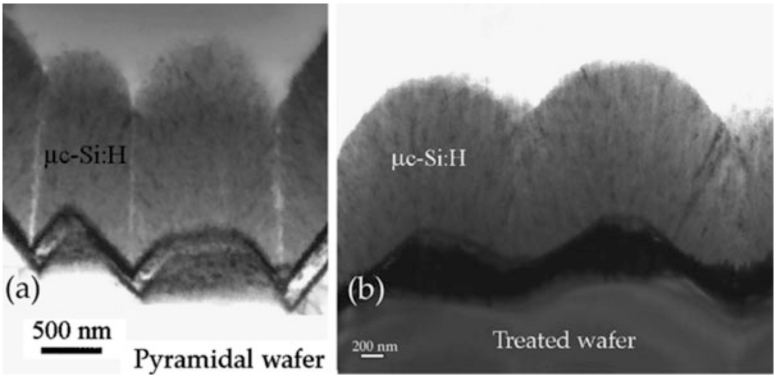

Fig. 38 TEM micrograph cross-section of a single-junction *p-i-n* solar cell deposited on a pyramidal wafer substrate. On the left, the “V-shaped” valleys of the substrate lead to “cracks” crossing the whole *p-i-n* device. On the right, the “U-shaped” substrate valleys result in a “crack” only in the last half of the μc-Si:H layer (Python et al. 2009)

affects the μc-Si:H solar cell performance significantly (Nasuno et al. 2001). If the substrate has a high texture, the columnar structures on the local surface could meet each other and lead to microvoids and microcracks as shown in Fig. 38 (Python et al. 2009), where the left image reveals the cross-section of a μc-Si:H solar cell deposited on a c-Si wafer having a pyramidal structured surfaces with sharp angles at the bottom of valleys called “V” shape, while the right one is on the substrate with chemically smoothed the surface to remove the sharp peaks and valleys and make the surface having the textures of “U” shape. It is clear that the μc-Si:H deposited on the “V” shaped substrate has microcracks all the way going through the entire thickness of the sample, while not much microcracks can be observed in the μc-Si:H solar cell on the “U” shaped substrate. The texture-induced microcracks not only reduce μc-Si:H solar cell efficiency, but also cause ambient degradation from the postdeposition impurity diffusion. Based on the results above, Bailat et al. proposed using a plasma treatment to smooth the textures on ZnO substrates and demonstrated a noticeable improvement in μc-Si:H solar cell performance (Bailat et al. 2006).

The group in AIST, Japan, invented an electric flat and optical textured back reflector as shown in Fig. 39 (Sai et al. 2011, 2012), which is made of two materials with different dielectric constants and forms a flat surface. The flat surface of the back reflector ensures microcrack-free deposition of μc-Si:H layers and the array made with two dielectrics scatters the light for light trapping. In reality, they used N-type a-Si:H and ZnO to form such back reflector (Fig. 40) and made a significant improvement in μc-Si:H solar cell performance as listed in Table 6 (Sai et al. 2011). Comparing the baseline cell on the flat substrate, the μc-Si:H solar cell deposited on the textured back reflector has a significant gain in the current due to the effective light trapping, but some losses in the V_{oc} and FF caused by the degradation of μc-Si:H material quality by the texture. Such detrimental effect becomes more serious in the cells on the normal grating substrate because of the highly structural texture. However, the solar cell on the flattened grating substrate shows the same V_{oc} and FF as the cell on the flat substrate, indicating the same high quality

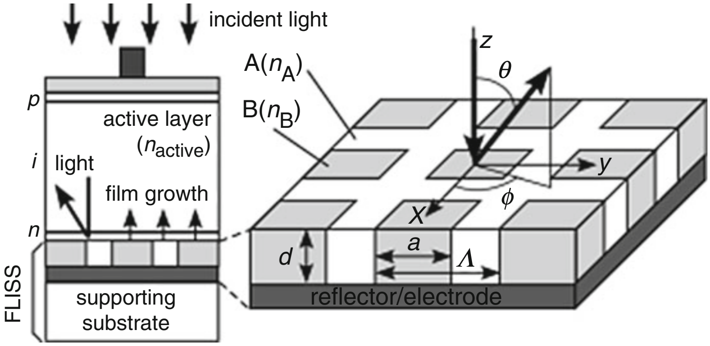

Fig. 39 Schematics of (left) a μc-Si:H solar cell on (right) an electric flat and optical textured back reflector (Sai et al. 2011)

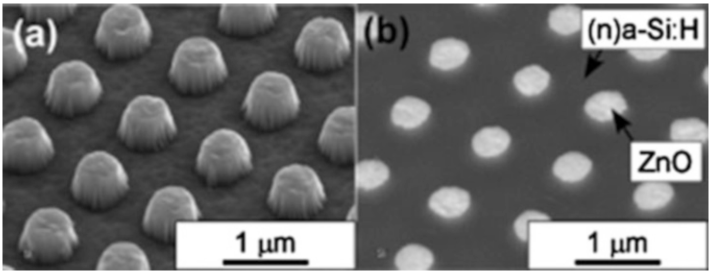

Fig. 40 SEM images of (**a**) the conventional a-Si:H and ZnO grating and (**b**) the flattened a-Si:H and ZnO grating (Sai et al. 2011)

Table 6 J-V characteristics of μc-Si:H solar cells deposited on different textured substrates (Sai et al. 2011)

Substrate	V_{oc} (V)	J_{sc} (mA/cm^2)	FF	Eff (%)
Flat	0.538	17.8	0.764	7.3
Texture	0.526	20.8	0.729	8.0
Grating	0.445	18.81	0.655	5.5
Polished grating	0.539	19.3	0.757	7.9

μc-Si:H as the one on the flat substrate. However, although the J_{sc} is higher than the cell on the conventional grating substrate, it is not as high as the one on the randomly textured reference substrates. Two issues might cause the less effectiveness of light trapping of the grating substrate: first the grating substrate might be effective in some wavelength region, but the sun light has a broad spectrum; second the N-type a-Si:H in the flattened back reflector absorbs some of the light reaching there. In this specific structure, the grating substrate does not have high response in the middle wavelength region, which was attributed to the absorption in the N-type a-Si:H layer in the back reflector. Such losses could be minimized when the μc-Si:H solar cells used as the

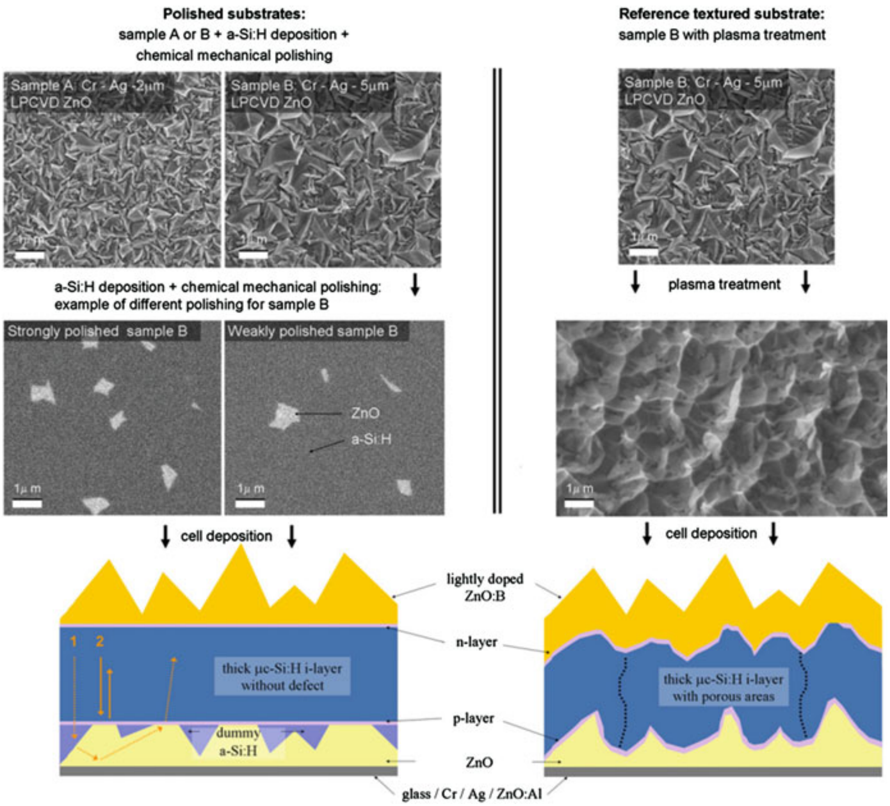

Fig. 41 SEM images of (left) polished substrates and (right) reference textured substrate during fabrication. Schematic drawings of cells grown on both types of substrates appear below. The colored arrows in the lower left panel illustrate loss in light trapping due to the flat ZnO/Si zones. The dashed lines in the lower right panel illustrate porous areas due to defective µc-Si:H growth (Söderströmn et al. 2012a)

bottom cell in multijunction solar cells. In addition, the antireflection effect of the ITO layer on the flat solar cell is not as effective as on textured solar cells.

Using the same principle, the Neuchal group made electric flat and optical texture back reflector by depositing an a-Si:H on randomly textured Ag/ZnO back reflector and then polishing the a-Si:H layer to use the remaining a-Si:H in the valleys to obtain a flat surface for high quality µc-Si:H deposition as shown in Fig. 41 (Söderströmn et al. 2012a, b). The left panel shows the SEM images of the surface morphologies before and after the polishing as well as the schematic of the µc-Si:H solar cell on such substrates; the right panel gives the same sequence of the plasma treatment process for smoothing the ZnO texture as the reference. In the polished substrates, the textures of the ZnO layer provide the effective light trapping and the flattened a-Si:H layer provides the flat surface for maintaining the µc-Si:H quality. In addition, the high peaks of the ZnO reached out of the filling

Table 7 Results of two co-deposited cells with a p-(μc-Si:H) doped layer optimized for polished substrates and for a cell with a p-doped μc-SiO_x:H layer optimized for textured substrates (Söderströmn et al. 2012a)

Type of substrate/p-doped layer	FF	V_{oc} (V)	J_{sc} (mA/cm^2)	Eff (%)
Textured/p-μc-Si:H	0.58	0.494	28.0	8.0
Polished A/p-μc-Si:H	0.67	0.520	27.3	9.5
Textured/p-μc-SiO_x:H	0.62	0.491	28.3	8.6

a-Si:H layer and flattened as well, which provide the electric contact for the current flow such that an undoped a-Si:H layer can be used as the filling materials without additional serious resistance. Table 7 summarizes the solar cell performances on different back reflectors. Comparing the first two rows of μc-Si:H solar cells, it is noted that the polished substrate results in a significant improvement in the FF and V_{oc}, which leads to an efficiency increase from 8.0% to 9.6%. The slightly low J_{sc} is caused by the additional absorption by the filling a-Si:H materials that result in a dip in the EQE at around 700 nm (Söderströmn et al. 2012a). It has also found that the detrimental effect of the substrate texture could be mitigated by using well-designed cell architectures. The use of a p-(SiOx:H) doped layer helps the cell to be less sensitive to locally porous material, which leads to an increase of the reference cell FF, as expected and demonstrated in the third row of Table 7. Nevertheless, the cell on the polished substrate with a p-(μc-Si:H) doped layer outperforms the reference cell in V_{oc} and FF. This result demonstrates that textures of the substrate indeed have a detrimental effect on μc-Si:H solar cell deposition and using an electric flat and optical textured substrate is an effective method to resolve this issue. Söderströmn et al. used the polished substrate to make a-Si:H/μc-Si:H/μc-Si:H triple-junction solar cells and achieved initial and stable solar cell efficiencies of 13.7% and 12.5% (Söderströmn et al. 2012b).

As discussed above, light trapping is an important technique for improving μc-Si:H solar cell performance. Beside the conventional light trapping schemes using randomly textured Ag/ZnO back reflectors for *n-i-p* structures and randomly textured AZO or BZO coated glass substrates for *p-i-n* structures, new advanced light trapping methods using plasmonic metal nanostructures (Pillai et al. 2007; Spinelli et al. 2012; Tan et al. 2013) and periodic photonic structures (Battaglia et al. 2012; Chen et al. 2015; Sai et al. 2009) have been extensively studied in recent years. Although some improvements have been achieved in the photocurrent gain, it is still not conclusive whether the modern light trapping approaches are better than the classic light trapping with randomly textured substrates and all of the record efficiencies for thin film silicon solar cells are achieved using the traditional randomly textured substrates. Because the advanced light trapping techniques are mainly dealing with the optical properties instead of the influence on μc-Si:H properties, it is not in the scope of this chapter. Readers are referred to the articles Battaglia et al. (2012), Chen et al. (2015), Pillai et al. (2007), Sai et al. (2009), Spinelli et al. (2012), and Tan et al. (2013).

Microcrystalline Silicon Germanium Alloy μc-SiGe:H

Similar to a-Si:H alloys, several microcrystalline silicon alloys have been studied for various applications. Used as the absorber layer to extend the infrared absorption, hydrogenated microcrystalline silicon germanium (μc-SiGe:H) is proposed by the ASIT group (Ganguly et al. 1996) and has been studied by the community (Carius et al. 1998; Matsui et al. 2006, 2007, 2009; Ni et al. 2014). Alloying Ge into μc-Si:H can reduce the bandgap further, which could expand the absorption edge beyond 1100 nm that is usually limited by the bandgap of the crystalline phase in μc-Si:H absorber layer. Figure 42 shows some EQE curves of μc-SiGe:H solar cells with various Ge contents, and Table 8 lists the cell performance parameters, where the μc-SiGe:H intrinsic layer is ~1 μm. It is noted that the long wavelength response is increased remarkable by the incorporation of Ge. The J_{sc} for the cell without Ge is 18.5 mA/cm^2, while the one with 20% Ge content goes up to 24.1 mA/cm^2 with a gain of 30% in the photocurrent density. However, a further increase in Ge content leads to a considerable degradation in all solar cell parameters. For Ge content of x = 40.2%, the decrease in V_{oc} is much greater than the band gap narrowing, indicating that the solar cell performance is dominated by the carrier recombination due to the increased dangling bond defects in the μc-SiGe:H *i*-layer. It is also noted that in the high Ge content solar cells, the short wavelength length response is reduced significantly by the increase of Ge related defects, which act as weak P-type doing and weaken the electric field in the region near the *p/i* interfaces. A proper O doping can

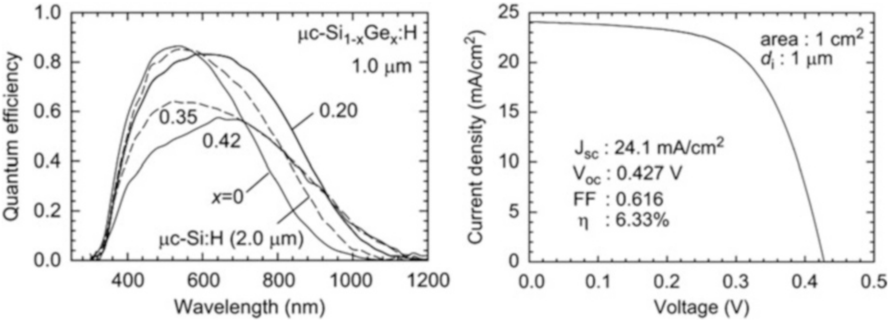

Fig. 42 (left) EQE curves of μc-$Si_{1-x}Ge_x$:H solar cells with various Ge contents, (right) J-V curve of a μc-$Si_{1-x}Ge_x$:H solar cell with 20% of Ge content (Matsui et al. 2009)

Table 8 Illuminated J–V parameters of the μc-$Si_{1-x}Ge_x$:H *p-i-n* solar cells with different Ge contents in the i-layer (Matsui et al. 2009)

G content x	Thickness (μm)	V_{oc} (mV)	J_{sc} (mA/cm^2)	FF	Eff (%)
0.00	1.0	560	18.5	0.730	7.75
0.20	1.0	412	23.6	0.663	6.12
0.35	1.0	214	20.6	0.380	1.67
0.42	0.9	195	18.8	0.354	1.29

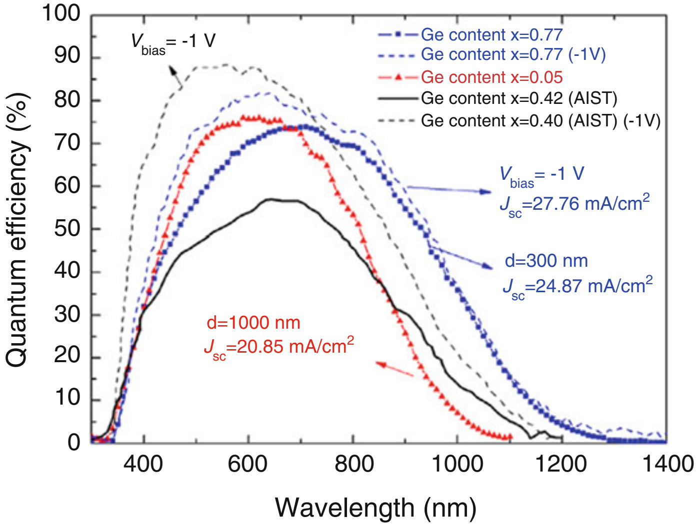

Fig. 43 Quantum efficiency spectra of μc-$Si_{1-x}Ge_x$:H *p-i-n* solar cells with different Ge contents (squares: x = 0.77, dashed blue line: x = 0.77 measured under reverse bias voltage of −1 V, triangles: x = 0.05). The μc-$Si_{1-x}Ge_x$:H solar cells with champion response in the long-wavelength regions are shown for comparison (solid black line: x = 0.42 from AIST, see; dashed black line: x = 0.40 measured under reverse bias voltage of −1 V (Ni et al. 2014)

compensate such P-type defect and improve the cell performance. Ni et al. (2014) used a proper ion bombardment technique to improve the μc-SiGe:H quality with a high Ge content up to 77% and made reasonable good solar cells with the EQE extended to 1300 nm as shown in Fig. 43. The short wavelength EQE losses can be recovered by a reverse bias voltage to enhance the electric field for carrier collection as shown in Fig. 43, confirming the losses is indeed from recombination.

As a narrow bandgap material, μc-SiGe:H can extend the long wavelength response of solar cells. However, the overall material quality still needs to be further improved. Currently, the losses in FF and V_{oc} with the incorporation of Ge are more than the gain in the current for the efficiency contributions; therefore, a higher efficiency with μc-SiGe:H as bottom cell than with μc-Si:H bottom cell has not been achieved in double- and triple-junction solar cells. There might be a hope to use μc-SiGe:H in quadruple-junction solar cells to obtain a high efficiency.

High Rate Deposition of μc-Si:H

Because μc-Si:H solar cells needs the absorber layer around 3–5 μm, a high rate deposition of μc-Si:H is a critical technology for a-Si:H and μc-Si:H based multi-junction solar cell application. As previously discussed, high hydrogen dilution is the key parameter for μc-Si:H deposition, but high hydrogen dilution normally reduces the deposition rate; one could increase the deposition rate by increasing the RF power, but a high RF power causes high energy bombardments and reduces the material quality. Therefore, using the conventional RF PECVD is difficult to achieve high rate deposition for μc-Si:H materials. Over the years, many techniques have been explored for μc-Si:H depositions including RF PECVD, VHF PECVD, microwave PECVD, how-wire CVD, and Photo-CVD. The most successful and widely used method for high rate μc-Si:H is VHF PECVD in the high power, high pressure depleting regime. Therefore, we present some details of this method below.

The Neuchatel group was the pioneer using VHF PECVD for thin film silicon deposition (Meier et al. 1994a, b, 1996; Shah et al. 2003). As shown in the previous chapter, under the same excitation power, the deposition rate increases with the excitation frequency, which is attributed the high dissociation rate with high frequency and therefore a high plasma density. The high dissociation rate results in a high atomic hydrogen flux intensity to the growth surface and promotes the formation of μc-Si:H. Therefore, VHF PECVD is the mostly used method for high rate μc-Si:H solar cells. Because of the shortened wavelength of VHF electromagnetic wave with the increase of frequency, the large area uniformity is a challenge in large area VHF PECVD system design. A compromised frequency for large area PECVD deposition and good μc-Si:H quality is in the range of 40 MHz to 80 MHz, and 60 MHz or 65 MHz is often selected. With VHF PECVD, high-quality μc-Si:H materials can be made at the deposition rate in the range of 2–3 nm/s, which can reach the same production efficiency as a-Si:H and a-SiGe:H multijunction solar panel production.

The group at AIST, Japan, invented high pressure depleting (HDP) mode in RF PECVD for high rate μc-Si:H deposition (Fukawa et al. 2001; Gou et al. 1998; Kondo 2003). The logic is that a high RF power is needed for achieving a high rate deposition, but the high RF power generates high energy ions that bombard the growth surface and results in a high defect density in the deposited materials; to reduce the high energy ion bombardments, one could increase the process pressures to increase the collision of ions during the transport to the growth surface and reduce the ion energy. A high RF power also increases the dissociation rate and produces additional hydrogen atoms by breaking SiH_4 molecules, especially at the depleting conditions where all of the active gases are dissociated for film deposition. In this case, the required hydrogen dilution for microcrystalline formation is reduced because of the extra atomic hydrogen from SiH_4 molecules. Based on the Paschen curve, one needs to reduce the gap between the cathode and the anode for getting stable plasma when the pressure is increased. Therefore, the electrode gap is normally narrower when the HDP mode is used. For example, a gap of 4–6 cm could be used when the deposition pressure is at 1–2 torr, and it should be reduced to around or below ~1.0 cm when the pressure is increased to >5 torr.

Another method to reduce the ion energy in the high RF power deposition is to insert a mesh electrode in front of the substrate (Kondo 2003; Matsui and Kondo 2013); by biasing or grounding the mesh electrode, the ion energy can be controlled and the deposited material quality can be improved. However, the mesh electrode blocks some species from reaching the growth surface and therefore it reduces the deposition rates in some degrees. Figure 44 shows deposition rates as a function of RF power in an RF PECVD system with and without the mesh electrode. It is noted

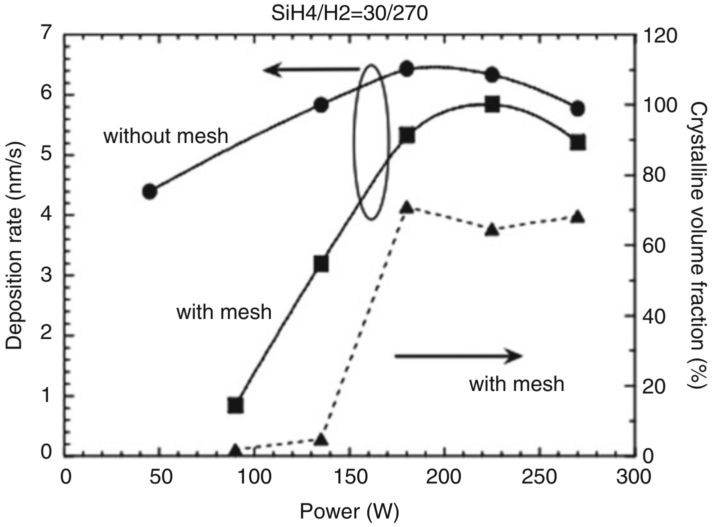

Fig. 44 The deposition rate and the crystalline volume fraction as a function of the power under high-pressure depletion conditions using VHF plasma with and without the mesh. The film structure is shown only the case with the mesh because the film structure without using the mesh is always amorphous (Kondo 2003)

that in the un-depleting regime, the deposition rate increases with the RF power due to the increase of dissociation rate and the plasma density, and then it saturates and starts to decrease with the RF power, indicating a depleting of the active gases where the increased atomic hydrogen etches the growth surface and reduces the deposition rates. Figure 44 also plots the crystallinity as a function of RF power, showing the sharp increase of crystallinity when the depleting mode is reached. Figure 45 shows the defect density measured by electron spin resonance (ESR) versus the deposition rate in three cases of the conventional, HPD,and meshed RF PECVD depositions. In the conventional RF PECVD, the defect density increases sharply with the deposition rate, the slope of defect increase with RF power becomes shallower in the HPD case, and much lower defect density is obtained with the meshed configuration, indicating the advantages of the HPD and meshed PECVD depositions.

It has also been found that an optimized design of the cathode and gas distribution/pumping systems can also improve the μc-Si:H material quality and solar cell efficiency. A multihole cathode also designed by the ASIT group is shown in Fig. 46. Using this system (Niikura et al. 2004, 2006), the defect density was further reduced to ~5 × 10^{15} cm^{-3} for μc-Si:H deposited at 8 nm/s as shown in Fig. 47 (Niikura et al. 2004). Panasonic has also designed a similar system named Localized Plasma Confinement (LPC-CVD) (Terakawa 2013) and improved their large area a-Si:H/μc-Si:H module efficiency significantly at a high deposition rate. A group at Osaka University used an atmosphere pressure 150 MHz VHF-PECVD to increase the deposition rate of μc-Si:H to 80 nm/s and demonstrated the good material quality, but the techniques have some difficulty for large area deposition (Kakiuchi et al. 2009).

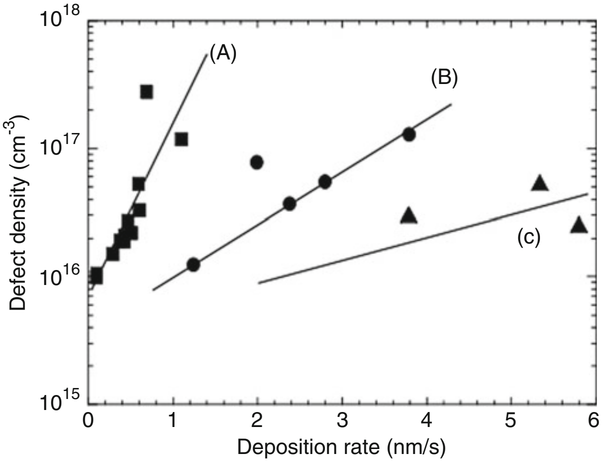

Fig. 45 Defect density measured by ESR as a function of deposition rate using three different methods; (**a**) conventional method, (**b**) high pressure depletion method, and (**c**) triode method (Kondo 2003)

Strobel et al. (2015) increased the VHF frequency to 140 MHz, which could increase the deposition further, but also facing large area uniformity issue.

High rate deposition μc-Si:H is still a bottle neck for a-Si:H/μc-Si:H based solar cell module production with large area systems. By compromising the deposition rate, uniformity, material quality, and the complexity of large system design, a commonly used production technique is VHF PECVD under the HPD regime with a narrow gap space between the cathode and the substrate. The excitation frequency is in the range between 40 MHz and 80 MHz with a deposition rate in the order of 1–2 nm/s. For example, TEL Solar's production machine uses 40 MHz VHF PECVD.

μc-Si:H Thin Film Silicon Solar Cell Design and Optimization

A good material quality is the necessary condition, but not the sufficient condition for achieving high efficiency solar cells. The optimizations in device design and fabrication are all important procedures for achieving high efficiency solar cells. For μc-Si:H solar cells, several topics as directly related to the material properties and their influence on cell performance have been addressed above, such as the hydrogen dilution profile, improving the compactness of μc-Si:H materials, and light trapping. Below, we discuss two other important aspects: the doped layer and the interface.

Doped Layer

In the early time, B-doped and P-doped a-Si:H layer are used as the *p* and *n* layers, respectively, in *p-i-n* and *n-i-p* structured thin film solar cells. The B-doped a-Si:H

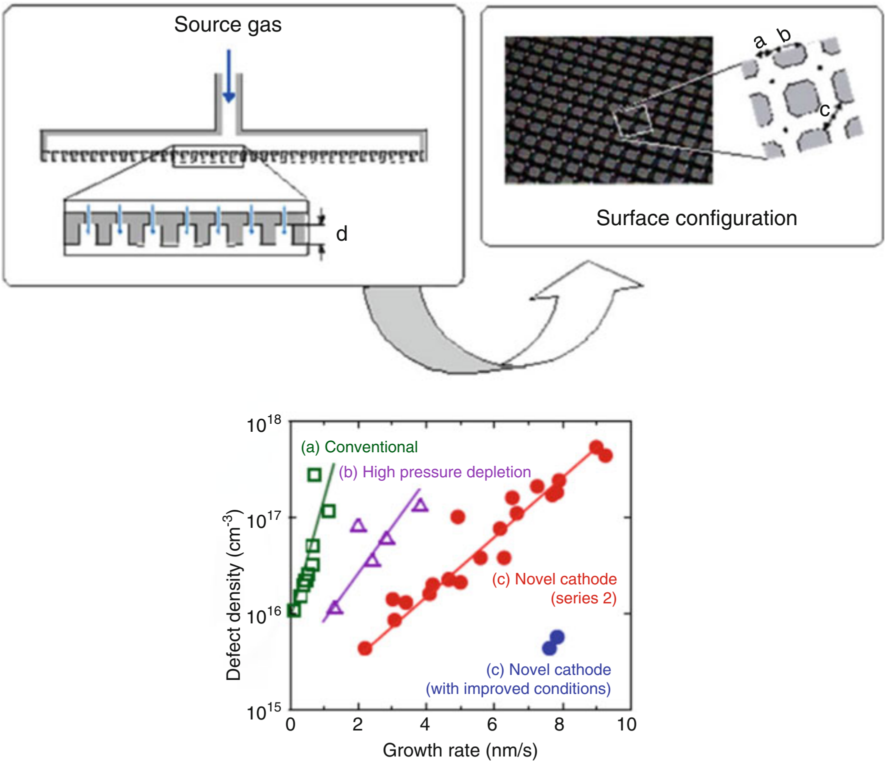

Fig. 46 (upper) A multihole cathode designed by the ASIT group, and (lower) the defect density versus the deposition rate with various methods (Niikura et al. 2004, 2006)

Fig. 47 The spectra of the μc-SiOx:H layer is deconvoluted in an a-SiOx:H peak (dashed line) and a μc-Si:H peak (dotted line) to calculate the crystalline volume fraction (Lambertz et al. 2011)

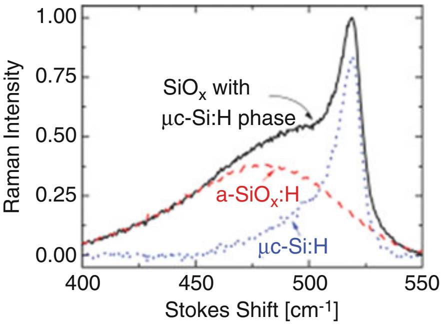

was deposited with B_2H_6 as the doping gas and PH_3 as the N-type doping gas. Because B_2H_6 is not stable and could be thermally dissociated in the cylinder, the process parameter could shift with time. In addition the bandgap of B-doped a-Si:H narrows with the increase of B content, and it reduces the short wavelength response of solar cells. Alternatively, B-doped a-SiCx:H has been widely used as the *p* layer in a-Si:H and μc-Si:H solar cells with Trimethylboron (TMB) as the doping gas

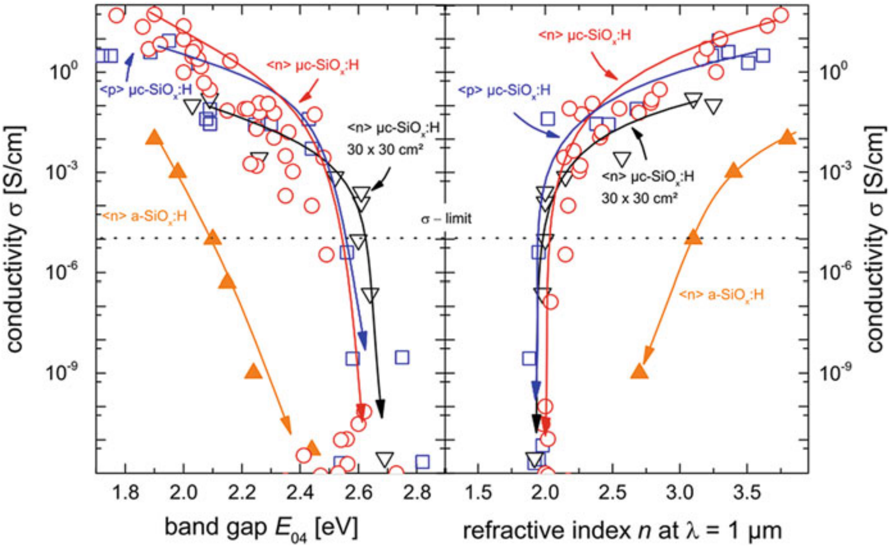

Fig. 48 The electrical conductivity values for μc-SiOx:H n-type (circles, triangles) and p-type (squares) films as a function of the band gap energy E_{04} (left) and as a function of the refractive index n (right), respectively (Lambertz et al. 2013)

(Tawada et al. 1982; Komuro et al. 1984). The group at United Solar invented B-doped μc-Si:H:F using BF_3 as the doping gas and improved the V_{oc} significantly in a-Si:H, a-SiGe:H and μc-Si:H solar cells (Guha et al. 1986). Nowadays, for high efficiency μc-Si:H solar cells, the doped layers (both *p*-layer and n-layer) use microcrystalline silicon oxide μc-SiO$_x$:H (Buehlmann et al. 2007; Bugnon et al. 2012; Hou et al. 2015; Janthong et al. 2012; Lambertz et al. 2011, 2012, 2013; Smirnov et al. 2012), which is also called nc-SiO$_x$:H. Therefore, we will mainly discuss μc-SiO$_x$:H below.

μc-SiO$_x$:H materials are a mixture of nanometer sized Si grains (nc-Si) embedded in an a-SiO$_x$:H matrix. Figure 47 shows a Raman spectrum of μc-SiO$_x$:H material with the deconvolution with c-Si TO mode and the a-SiOx:H component (Lambertz et al. 2011). Such a two-phase structure results in the following unique properties. First, the crystalline phase is mainly nanometer sized silicon, where the doping efficiency could be high and form high conductive paths for current flow, especially in the vertical direction to the sample surface. The high doping efficiency and high conductivity establish the fundamental of the doped layers for solar cell application. The material can be doped in both N-type and P-type as shown in Fig. 48. Second, the a-SiO$_x$:H tissue has a wide optical bandgap as measured by E_{04}, where the absorption coefficient equals 10^4 cm^{-1}, and low absorption coefficients for the window layer application; it greatly improves the short wavelength response on solar cells as shown in Fig. 49, which shows the performance a μc-Si:H solar cell with the μc-SiO$_x$:H p-layer. One can see that the EQE at the short wavelength is very high, benefited from the low absorption in the μc-SiO$_x$:H *p*-layer and the additional

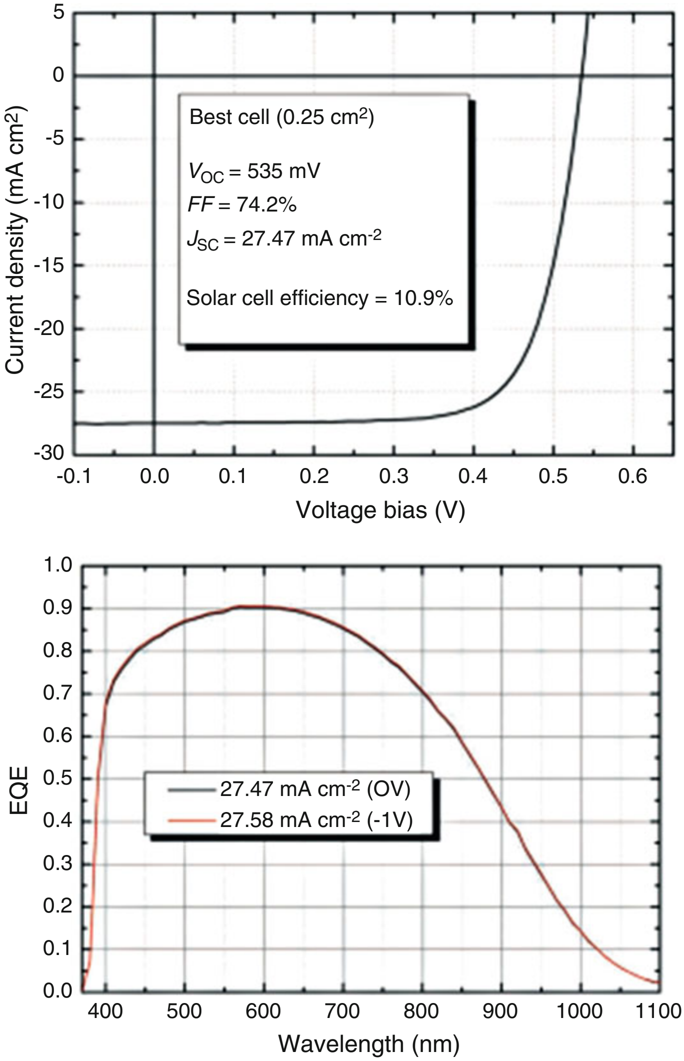

Fig. 49 J-V characteristics and EQE curves under 0 V and −1 V of the best-performing single-junction *p*-*i*-*n* μc-Si:H solar cell (0.25 cm^2) with an intrinsic layer thickness of 2 μm deposited at 3 Å/s with optimized SiOx:H doped layers and interfaces along with an anti-reflective coating at the air/glass interface (Bugnon et al. 2012)

antireflection coating effect. Using a μc-SiOx:H *n*-layer also improves μc-Si:H solar cell performance, by reducing the long wavelength loss absorbed in the *n*-layer, enhancing the light trapping and preventing microshunting caused by the textured substrates.

The refractive index n of μc-SiO$_x$:H changes with the O content and can be tuned between 3.5 and 2.0 as shown in Fig. 48, which can act as the dielectric layer for light trapping and light management such as an intermedium reflection layer in multi-junction solar cells by reflecting some portion of light back to the a-Si:H top cell to achieve the designed current mismatching between the subcells (Janthong et al. 2012; Jung et al. 2014; Lambertz et al. 2013; Yamamoto et al. 2005). Because of the functions as doped layer and intermedium refection layer, Yan et al. (2011) used it as the dual-function layer of n layer and intermedium reflection layer in a-Si:H/a-SiGe:H/μc-Si:H triple-junction solar cells and achieved a record efficiency of 16.3%.

Interface Layers

Except for the intrinsic and doped layers, the interfaces between the intrinsic and doped layers also affect the cell performance significantly. Mai et al. incorporated an intrinsic μc-Si:H buffer layer at *p/i* interface prepared by hot-wire CVD process into PECVD fabricated μc-Si:H solar cells and improved the V_{oc} by weakening the ion bombardment damage at the *p/i* interface (Mai et al. 2006). the J-V characteristic curves the cells with and without the hot-wire CVD buffer layer are shown in the Fig. 50, which demonstrates the effectiveness of the hot-wire deposited buffer layer in the improvement of V_{oc} and results in an record efficiency of 10.3% at the time.

An intrinsic a-Si:H buffer layer can also improves μc-Si:H solar cell performance by reducing the microshunt path, blocking the diffusion of doping atom into the intrinsic layer (Yue et al. 2008; Bai et al. 2015a). Since μc-SiO$_x$:H *p* layer has been widely used as the window layer in μc-Si:H solar cells, it is logical to use an a-SiO$_x$:H or μc-SiO$_x$:H as the *p/i* buffer layer. Figure 51 depicts the illuminated J-V characteristics and EQE curves of two μc-Si:H single-junction solar cells with and without the intrinsic μc-SiO$_x$:H buffer, which show an noticeable improvement in the cell performance (Bai et al. 2015a).

It was also found that the use of intrinsic silicon oxide as a buffer layer at the *p/i* interface of μc-Si:H solar cells provided significant advantages (Bugnon et al. 2014) in μc-Si:H solar cells: an improvement in carrier collection in the blue region of the spectrum is systematically observed, as shown in Fig. 52, which might result from

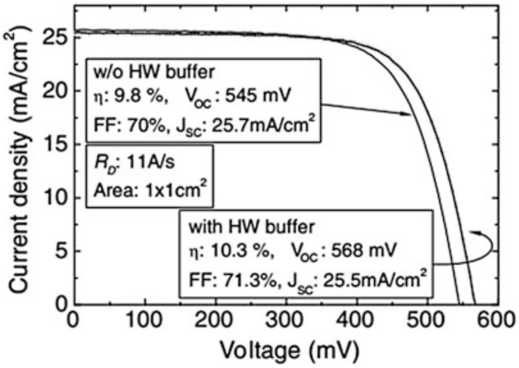

Fig. 50 J-V characteristics of μc-Si:H single-junction solar cells with and without a hot wire CVD deposited *p/i* buffer, where the bulk *i*-layer was deposited by PECVD at 1.1 nm/s (Mai et al. 2006)

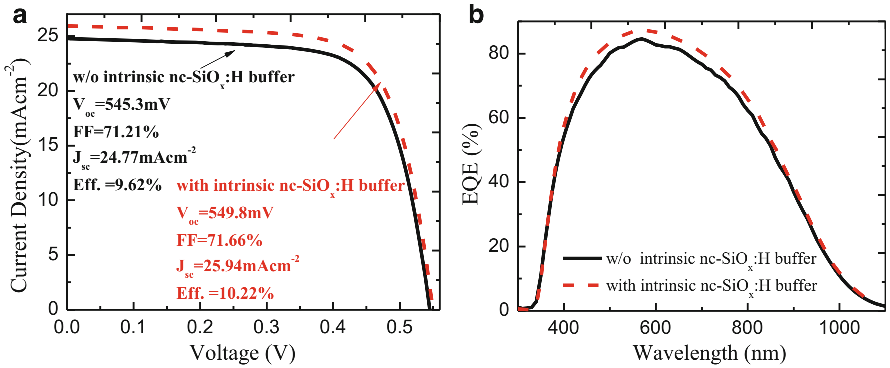

Fig. 51 (**a**) Illuminated J-V characteristics and (**b**) EQE curves of μc-Si:H single-junction solar cells with and without intrinsic μc-SiO$_x$: H buffers (Bai et al. 2015a)

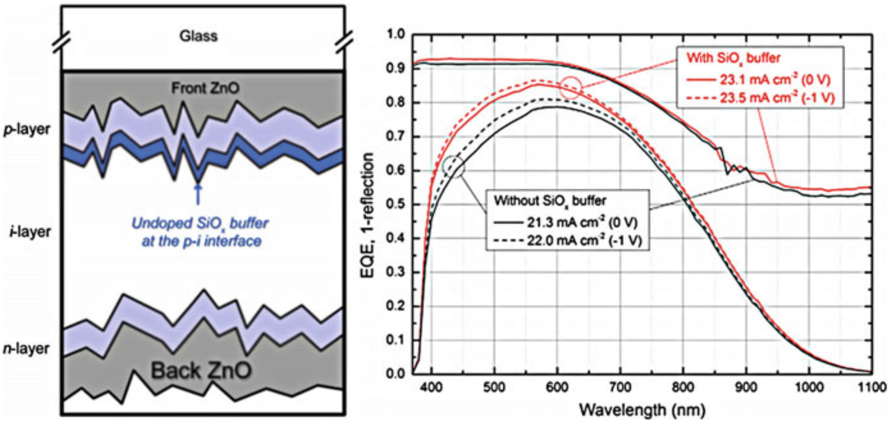

Fig. 52 Sample scheme of a *p-i-n* cell with a SiO$_x$:H buffer at the *p/i* interface, and the EQE of the *p-i-n* μc-Si:H solar cells, with (red) and without (black) the SiO$_x$ buffer layer at the p/i interface (Bugnon et al. 2014)

the reduction of B contamination from the *p*-layer and the change of crystalline structure in the *i*-layer near the *p/i* interface.

An intrinsic or N-type a-Si:H buffer layer inserted between the μc-Si:H intrinsic and nc-SiO$_x$:H *n* layers can also improve the cell performance by reducing the bandgap mismatching, blocking the diffusion of doping atoms into the intrinsic layer, and removing the micro-shunt paths (Bai et al. 2015b; Söderström et al. 2008). An example is shown in Fig. 53 (Bai et al. 2015b), where a series of μc-Si:H single-junction solar cells were made with the same condition except with different *n*-type a-Si:H buffer thicknesses (0, 4, 6, 8, and 10 nm). It evidently shows that as the buffer layer thickness gradually increased from 0 nm to 10 nm, the V$_{oc}$ of the samples maintained nearly the same value (about 0.545 V). However,

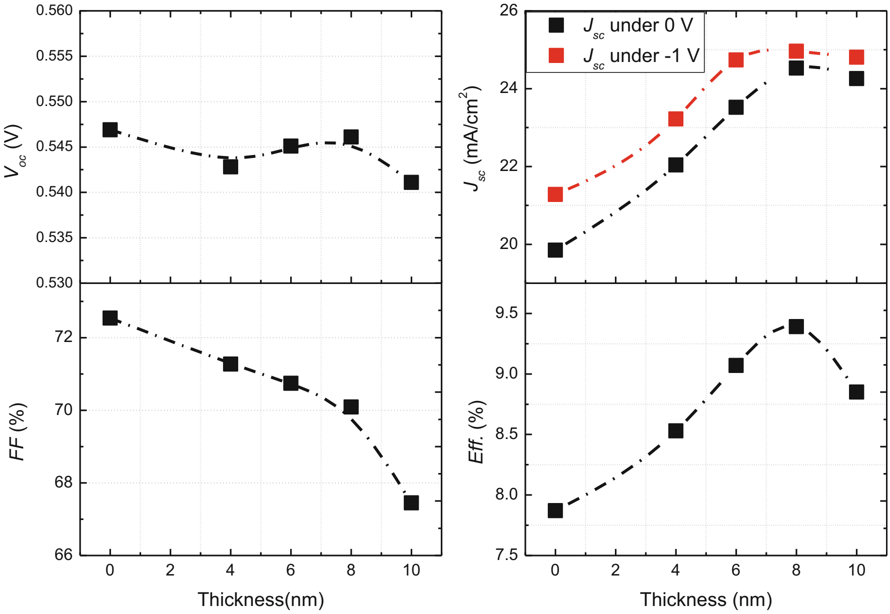

Fig. 53 Device parameters of single-junction of μc-Si:H solar cells with different thicknesses of the n-a-Si buffer layers (Bai et al. 2015b)

the FF continuously decreased from 72.54% to 67.45%, which might be due to the additional series resistance, while the J_{sc} values obtained from the EQE at 0 V and −1 V gradually increased with the buffer thickness until it reached the maximum at the 8 nm thickness, after which it slightly decreased. The increase in J_{sc} values mainly originates from the increases of the long-wavelength response. The variation trend of efficiency (Eff) with the buffer layer thickness values is similar to that of J_{sc}, an experimental observation proving that the J_{sc} variation has the strongest influence on the overall power output in this study. A maximized efficiency of 9.39% was achieved when an *n*-type a-Si:H buffer layer with a thickness of 8 nm is inserted between the μc-Si:H intrinsic and *n*-type nc-SiO_x:H layers.

High Efficiency μc-Si:H Single-Junction Solar Cell

From the results above, one may realize that the design and optimization of μc-Si:H solar cell efficiency is a complicated scientific and engineering process. A better understanding of the deposition process and its correlation with the material properties helps to design a cell fabrication process to deposit high quality materials; an optimized device design with the best materials and well-controlled interface is also critical for solar cell performance. In addition, the transparent electrodes and back reflectors have to be optimized as well. Over the years, the community has made a

Table 9 The detail parameters of the highest efficiency single junction μc-Si:H solar cells

Year	Type	Institute	V_{oc} (V)	FF (%)	J_{sc} (mA·cm^{-2})	Eff. (%)
2006.03	p-i-n	Utrecht	0.52	74.0	25.9	10
2006.05	p-i-n	Juelich	0.568	71.3	25.5	10.3
2012.09	p-i-n	EPFL	0.535	74.2	27.47	10.9
2013.05	p-i-n	LGE	0.54	73.0	26.1	10.4
2015.06	p-i-n	Delft	0.552	72.6	25.6	10.2
2014.12	p-i-n	Nankai	0.552	71.76	26.6	10.54
2012.06	n-i-p	Uni-solar	0.543	69.1	28.15	10.56
2014.10	n-i-p	AIST	0.548	73.1	29.4	11.77

Note: Utrecht: (Gordijn et al. 2006); Juelich: (Mai et al. 2006); EPFL: (Bugnon et al. 2012); LGE: (Jung et al. 2014); Delft: (Tan et al. 2015); Nankai: (Zhang 2016); Uni-Solar: (Yue et al. 2012b); AIST: (Sai et al. 2015)

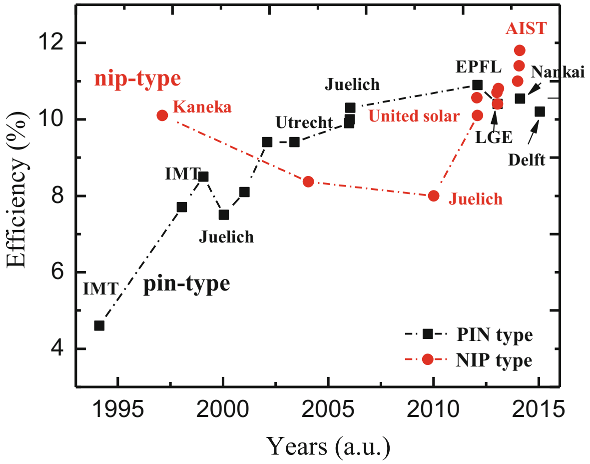

Fig. 54 The highest efficiency of *p-i-n* type and *n-i-p* type μc-Si:H single-junction solar cells achieved by different research institutions

significant progress in μc-Si:H cell efficiency improvement. Table 9 lists some selected high efficiencies achieved by different institutes, and Fig. 54 shows the progress made by the community. The best single-junction μc-Si:H solar cell efficiency is 11.8% achieved by the AIST group with certified performance characteristics shown in Fig. 55 (Sai et al. 2015).

A-Si:H and μc-Si:H Based Multijunction Solar Cell and Modules

As discussed above, the advantage of μc-Si:H over a-Si:H and a-SiGe:H as the absorber layer in solar cells is the extended absorption spectrum to the long wavelength for high photocurrent. Using μc-Si:H as the middle and bottom cells in multijunction solar cells can absorb the sun light in a wide range and achieve high solar cell efficiency. Over the years, several multijunction solar cell structures have

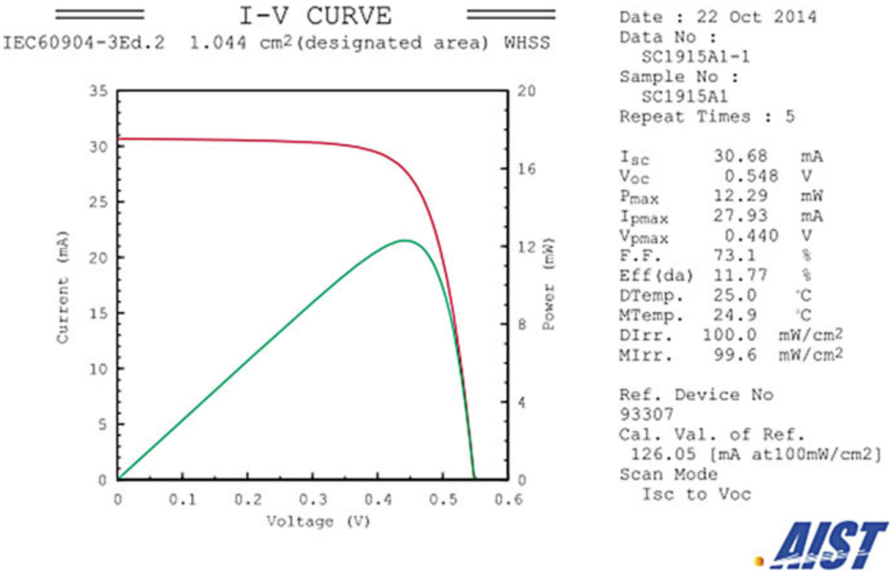

I-V CURVE

IEC60904-3Ed.2 1.044 cm2(designated area) WHSS

Date : 22 Oct 2014
Data No :
SC1915A1-1
Sample No :
SC1915A1
Repeat Times : 5

Isc	30.68	mA
Voc	0.548	V
Pmax	12.29	mW
Ipmax	27.93	mA
Vpmax	0.440	V
F.F.	73.1	%
Eff(da)	11.77	%
DTemp.	25.0	°C
MTemp.	24.9	°C
DIrr.	100.0	mW/cm2
MIrr.	99.6	mW/cm2

Ref. Device No
93307
Cal. Val. of Ref.
126.05 [mA at100mW/cm2]
Scan Mode
Isc to Voc

Fig. 55 J–V curves of the highest efficiency μc-Si:H cell independently confirmed by the CSM-RCPVT-AIST (V_{oc} = 0.548 V, J_{sc} = 29.4 mA / cm^2, FF = 0.731, Eff = 11.77%) (Sai et al. 2015)

been extensively studied. For example, Fig. 56 shows the commonly used *n-i-p* multijunction solar cells.

The design and fabrication of multijunction solar cells are much more complicated than single-junction solar cells. First, additional attentions must be paid to the current matching because the J_{sc} of a multijunction solar cell takes the smallest photocurrent density among the individual component cells. A proper design, the component cell thicknesses, and selection of the bandgap of the absorber layers in each component cell should be optimized to give the desired current matching for the best stable efficiency. Second, the connections between individual component cells need to be optimized to minimize the losses at the connection because the top cell *n*-layer and the bottom cell *p*-layer form an opposite p-n junction with the main *p-i-n* junctions, where the current flows through a tunneling and recombination process; therefore, the junction there is called the tunnel-junction. A good tunnel-junction should have a minimum voltage loss for high V_{oc} and a low resistance for good FF. Because these topics are more engineering, and the concept is similar to other multi-junction solar cells, we will not discuss the details here. But as expected the multijunction solar cells provide higher efficiency than single-junction solar cells. As mentioned previously, the highest initial efficiency for thin film silicon solar cells is 16.3% achieved using an a-Si:H/a-SiGe:H/μc-Si:H triple-junction structure with the J-V characteristics and EQE curves in Fig. 57 (Yan et al. 2011). Using an a-Si:H/μc-Si:H/μc-Si:H triple-junction structure, LG Solar have demonstrated an NREL confirmed 13.44% stable efficiency with the results shown in Fig. 58 (Kim et al. 2013). The progress

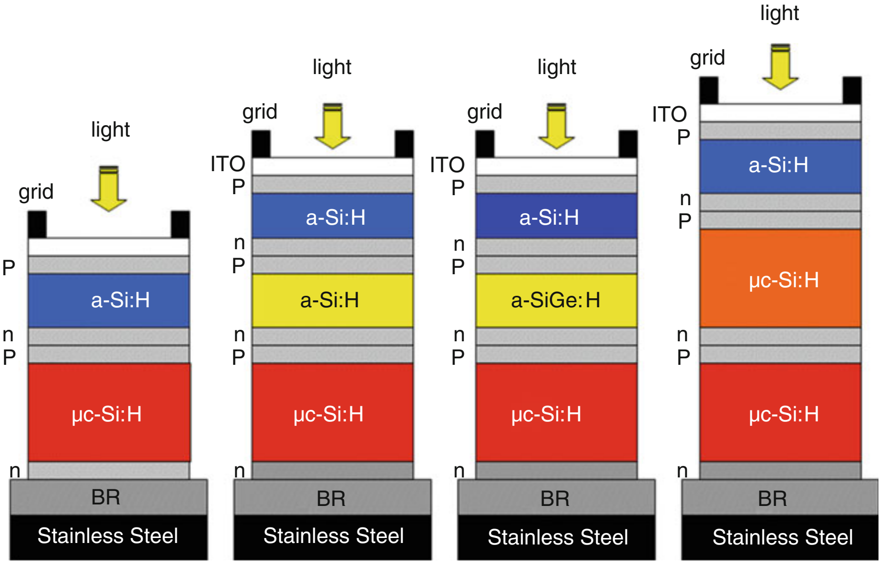

Fig. 56 Schematics of *n-i-p* multijunction solar cells with μc-Si:H in the bottom cell

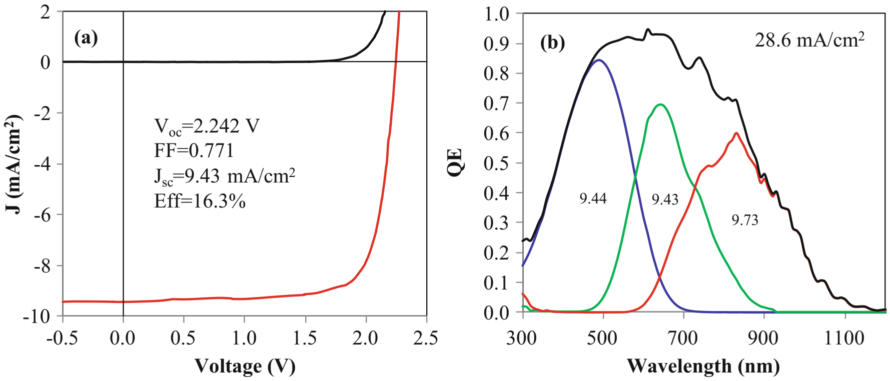

Fig. 57 (**a**) J-V characteristics and (**b**) EQE spectra of an a-Si:H/a-SiGe:H/μc-Si:H triple-junction solar cell with an initial efficiency of 16.3% (Yan et al. 2011)

of a-Si:H, a-SiGe:H and μc-Si:H multijunction solar cell efficiency made by the community is shown in Fig. 59. Although over 16% initial cell efficiencies have been achieved with both the *n-i-p* and *p-i-n* structures, the progress has been slowed down in recent years; especially the thin film silicon photovoltaic industry has been significantly shrunk. However, a remaining question for the thin film community is whether the thin film silicon solar cell efficiency has reached the

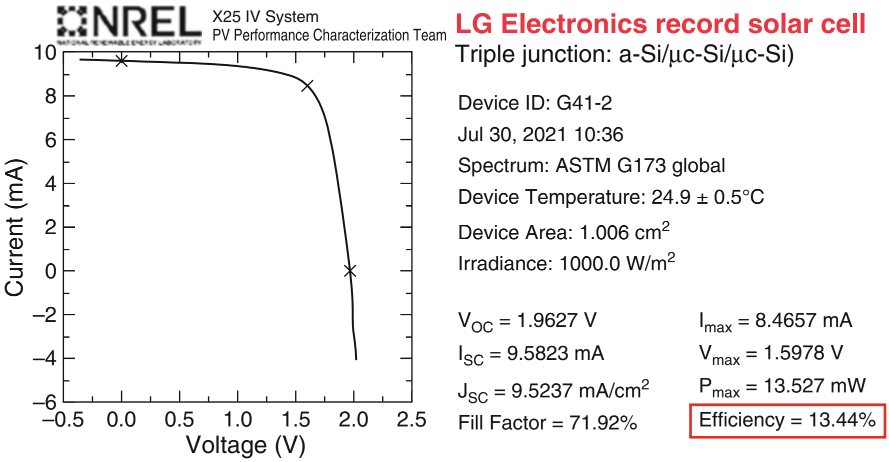

LG Electronics record solar cell

Triple junction: a-Si/μc-Si/μc-Si)

Device ID: G41-2

Jul 30, 2021 10:36

Spectrum: ASTM G173 global

Device Temperature: 24.9 ± 0.5°C

Device Area: 1.006 cm^2

Irradiance: 1000.0 W/m^2

V_{OC} = 1.9627 V

I_{SC} = 9.5823 mA

J_{SC} = 9.5237 mA/cm^2

Fill Factor = 71.92%

I_{max} = 8.4657 mA

V_{max} = 1.5978 V

P_{max} = 13.527 mW

Efficiency = 13.44%

Fig. 58 The established performance of the a-Si:H/μc-Si:H/μc-Si:H triple-junction solar cell after 1000 h light soaking. This new record was confirmed by NREL (Kim et al. 2013)

Fig. 59 The highest efficiency of a-Si:H/a-SiGe:H/μc-Si:H triple-junction solar cells achieved in different research institutions

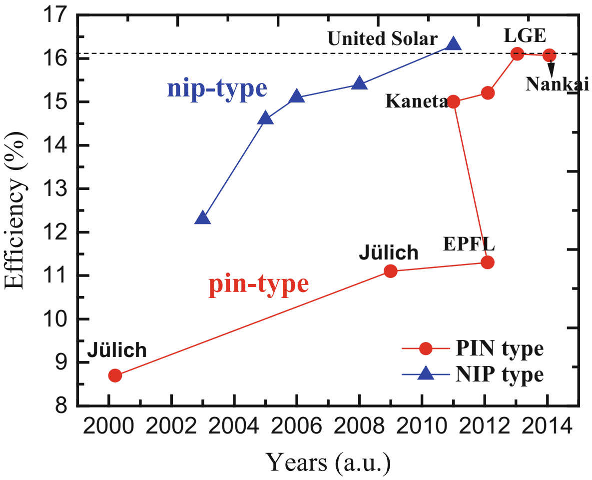

upper limit. Simulation studies have shown that with quadruple structures, around 20% cell efficiencies could be attained (Isabella et al. 2014).

a-Si:H and μc-Si:H multijunction solar cells have been also incorporated into production lines with increased module efficiency over a-Si:H and a-SiGe:H multi-junction product. Large area module efficiency has been steady improved. A stable large area (1.43 m^2) efficiency of 12.34% has been achieved by TEL Solar and confirmed by ESTI as shown in Fig. 60 (Cashmore et al. 2016).

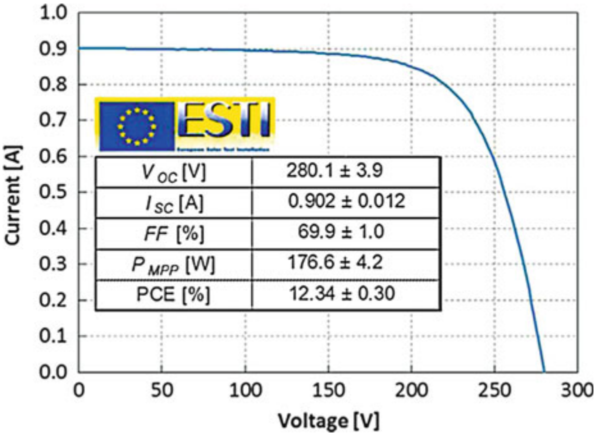

Fig. 60 Stabilized I-V curve and parameters of the record module (1.43 m^2))made by TEL Solar and certified by ESTI (Cashmore et al. 2016)

Summary

μc-Si:H is a unique material with nanometer sized crystallites embedded in amorphous silicon tissues. The complex in the material structure provides a great platform for material studies with rich physics and chemistry in the material deposition, characterization, and device applications. Here we reviewed the material properties with the main focuses to address the major issues affecting the μc-Si:H solar cell performance and the approaches to resolve these problems.

The key process parameter controlling the transition from a-Si:H to μc-Si:H is the hydrogen dilution. The μc-Si:H deposition needs a much higher hydrogen dilution than a-Si:H deposition. One of the interesting phenomena is the crystalline evolution: the μc-Si:H deposition starts with an a-Si:H incubation layer, follows with crystallite seed formation, grows cone-structured crystallite aggregations, and increases the crystalline volume fraction with film thickness. Such crystalline evolution with the film thickness has a negative impact on solar cell performance. To resolve this issue, a hydrogen dilution profile technique was invented with a very high hydrogen dilution to remove the a-Si:H incubation layer and growth μc-Si:H from the beginning, following a continually decreasing the hydrogen dilution to maintain a desired crystallinity distribution along the film thickness. The hydrogen dilution profiling technique is proven to be an effective method for high efficiency μc-Si:H solar cell deposition. The similar result can also be obtained by changing other parameters such as the excitation power in PECVD deposition with a high power at the initial deposition to promote the crystalline formation and gradually reducing the power during the deposition to maintain the same crystallinity.

μc-Si:H is more sensitive to impurity than a-Si:H especially to O. The tolerance for O in a-Si:H is in the level of 1–2 × 10^{19} cm^{-3}, but it is below 5 × 10^{18} cm^{-3} in μc-Si:H.

In addition, it is more sensitive to the normal doping elements of B and P. Therefore, a clean multichamber deposition system with pure gases is essential for high quality μc-Si:H materials and high efficiency solar cells. The O impurity can be compensated by adding a small amount of B called "microdoping." However, the window of "microdoping" is narrow and difficult to control. The impurities are not only incorporated during the deposition process, but also diffuse into the material after deposition and exposure to air for un-optimized μc-Si:H materials and solar cells, which cause the conductivity increase and solar cell efficiency decrease. To resolve the postdeposition impurity diffusion problem, one needs to optimize the process to deposit compact μc-Si:H materials to block the channel of impurity diffusion.

Light trapping is an effective method to improve the photocurrent density of μc-Si:H solar cells, hence efficiency. The *n-i-p* structured solar cells use a back reflector to achieve the light trapping, while the *p-i-n* cells use textured TCO such as AZO and BZO. Using an optimized Ag/ZnO back reflector, the current gain can be as high as 60%. However, the textures of the substrates could cause a negative effect on the μc-Si:H structure and quality. To resolve this issue, electric flat and optical textured back reflectors are invented. There is no conclusion whether a periodically structured back reflector is better than the randomly textured back reflector. Although some theories may provide a positive supporting, most high efficiency μc-Si:H based solar cells are made on randomly textured substrates.

The high rate deposition is a bottleneck for reducing the a-Si:H and μc-Si:H based thin film solar module production cost. The commonly used method for high rate deposition nowadays is VHF PECVD at the high power, high pressure depleting regime. The deposition rate could be in the range of 2–3 nm/s for good cell performance. Other techniques such as atmospheric VHF PECVD can make μc-Si:H at much high rate, but the scale-up to large area machine faces problems.

After the over 20 years of fundamental research and technology development, μc-Si:H single-junction solar cell efficiency has been over 11%, multijunction cell over 16%, and stable module efficiency over 12%. With the dramatic reduction of c-Si solar module price in recent years, thin film silicon PV product has lost the advantages in the market, especially in large scale utility level PV power station. However, the unique properties of the thin film silicon PV product such as the flexibility and light weight may keep the product in some niche market such as consumer electronic chargers, unmanned space vehicles and BIPV applications.

Looking forward for improving the thin film silicon cell and module efficiency, new materials and cells structures such as poly-Si thin film solar cells and modules will be discussed in the next chapter.

Acknowledgments The authors are grateful for the colleagues in the thin film silicon PV community. They have enjoyed very much for the collaborations with several institutions and sharing ideas and results through the international conferences such as the MRS, ICANS, IEEE-PVSEC, and EU-PVSEC. BY acknowledges the hospitality of the Nankai University.

References

L. Bai, B. Liu, J. Zhao, et al., J. Appl. Phys. **117**, 175309 (2015a)

L. Bai, B. Liu, Q. Huang, et al., Sol. Energy Mater. Sol. Cells **140**, 202 (2015b)

J. Bailat, E. Vallat-Sauvain, L. Feitknecht, C. Droz, A. Shah, J. Non-Cryst. Solids **1219**, 299–302 (2002)

J. Bailat, D. Dominé, R. Schlüchter, J. Steinhauser, S. Fay, F. Freitas, C. Bücher, L. Feitknecht, X. Niquille, T. Tscharner, A. Shah, C. Ballif, Proc. 4th World Conf. on Photovoltaic Energy Conversion (Hawaii, 2006), p. 1533

C. Battaglia, C.-M. Hsu, K. Söderström, J. Escarre, F.-J. Haug, M. Charriere, M. Boccard, M. Despeisse, D.T.L. Alexander, M. Cantoni, Y. Cui, C. Ballif, ACS Nano **6**, 2790 (2012)

M.H. Brodsky, M. Cardona, J.J. Cuomo, Phys. Rev. B **16**, 3556 (1977)

P. Buehlmann, J. Bailat, D. Domine, A. Billet, F. Meillaud, A. Feltrin, et al., Appl. Phys. Lett. **91**, 143505 (2007)

G. Bugnon, G. Parascandolo, T. Söderström, P. Cuony, M. Despeisse, S. Hänni, J. Holovský, F. Meillaud, C. Ballif, Adv. Funct. Mater. **22**, 3665 (2012)

G. Bugnon, G. Parascandolo, S. Hänni, et al., Sol. Energy Mater. Sol. Cells **120**, 143 (2014)

E. Bustarret, M.A. Hachicha, M. Brunel, Appl. Phys. Lett. **52**, 1675 (1988)

R. Carius, J. Folsch, D. Lundszien, L. Houben, F. Finger, Mater. Res. Soc. Symp. Proc. **507**, 813 (1998)

J.S. Cashmore, M. Apolloni, A. Braga, O. Caglar, V. Cervetto, Y. Fenner, S. Goldbach-Aschemann, C. Goury, J.E. Hötzel, T. Iwahashi, J. Kalas, M. Kitamura, M. Klindworth, M. Kupich, G.-F. Leu, J. Lin, M.-H. Lindic, P.A. Losio, T. Mates, D. Matsunaga, B. Mereu, X.-V. Nguyen, I. Psimoulis, S. Ristau, T. Roschek, A. Salabas, E.L. Salabas, I. Sinicco, Sol. Energy Mater. Sol. Cells **144**, 84 (2016)

P. Chen, G. Hou, Q. Fan, J. Ni, J. Zhang, Q. Huang, X. Zhang, Y. Zhao, Sol. Energy Mater. Sol. Cells **143**, 435 (2015)

Y.-B. Chung, D.-K. Lee, J.-S. Lim, N.-M. Hwang, Sol. Energy Mater. Sol. Cells **95**, 211 (2011)

R.W. Collins, A.S. Ferlauto, G.M. Ferreira, C. Chen, J. Koh, R.J. Koval, Y. Lee, J.M. Pearce, C.R. Wronski, Sol. Energy Mater. Sol. Cells **78**, 143 (2003)

L.R. Dahal, J. Li, J.A. Stoke, Z. Huang, A. Shan, A.S. Ferlauto, C.R. Wronski, R.W. Collins, N.J. Podraza, Sol. Energy Mater. Sol. Cells **129**, 32 (2014)

P. Debye, P. Scherrer, Physik. Z. **17**, 277 (1916)

C. Droz, E. Vallat-Sauvain, J. Bailat, L. Feitknecht, J. Meier, A. Shah, Sol. Energy Mater. Sol. Cells **81**, 61 (2004)

T. Dylla, F. Finger, E.A. Schiff, Appl. Phys. Lett. **87**, 032103 (2005)

F. Finger, in *Thin-Film Silicon Solar Cells*, ed. by A. Shah (Ed), (EPFL Press, Lausanne, 2010) Chapter 3

M. Fukawa, S. Suzuki, L. Guo, M. Kondo, A. Matsuda, Sol. Energy Mater. Sol. Cells **66**, 217 (2001)

G. Ganguly, T. Ikeda, T. Nishimiya, K. Saitoh, M. Kondo, A. Matsuda, Appl. Phys. Lett. **69**, 4224 (1996)

A. Gordijn, J.K. Rath, R.E.I. Schropp, Prog. in Photovoltaics: Res. and Appl **14**, 305 (2006)

Q. Gu, Q. Wang, E.A. Schiff, Y.-M. Liand, C.T. Malone, J. Appl. Phys. **76**, 2310 (1994)

L. Guo, M. Kondo, M. Fukawa, K. Saitoh, A. Matsuda, Jpn. J. Appl. Phys. **37**, L1116 (1998)

S. Guha, J. Yang, P. Nath, M. Hack, Appl. Phys. Lett. **49**, 218 (1986)

S. Guha, J. Yang, B. Yan, Sol. Energy Mater. Sol. Cells **119**, 1 (2013)

X. Han, G. Hou, X. Zhang, C. Wei, G. Li, J. Zhang, X. Chen, D. Zhang, J. Sun, Y. Zhao, X. Geng, Sol. Energy Mater. Sol. Cells **94**, 254 (2010)

Q. Huang, Y. Liu, S. Yang, Y. Zhao, X. Zhang, Solar Ener. Mater. & Sol. Cells **103**, 134 (2012)

G. Hou, J. Fang, Q. Fan, C. Wei, J. Ni, X. Zhang, Y. Zhao, Sol. Energy Mater. Sol. Cells **134**, 395 (2015)

J. Hüpkes, H. Zhu, J.I. Owen, G. Jost, E. Bunte, Thin Solid Films **520**, 1913 (2012)

O. Isabella, A.H.M. Smets, M. Zeman, Sol. Energy Mater. Sol. Cells **129**, 82 (2014)

Z. Iqbal, S. Veprek, J. Phys. C **15**, 377 (1982)

B. Janthong, A. Hongsingthong, T. Krajangsang, L. Zhang, P. Sichanugrist, M. Konagai, J. Non-Cryst. Solids **358**, 2478 (2012)

S.J. Jung, B.J. Kim, M. Shin, Sol. Energy Mater. Sol. Cells **121**, 1 (2014)

H. Kakiuchi, H. Ohmi, K. Ouchi, K. Tabuchi, K. Yasutake, J. Appl. Phys. **106**, 013521 (2009)

S. Kasouit, S. Kumar, R. Vanderhaghen, P. Roca i Cabarrocas, I. French, J. Non-Cryst. Solids **113**, 299–302 (2002)

S. Kim, J.-W. Chung, H. Lee, J. Park, Y. Heo, H.-M. Lee, Sol. Energy Mater. Sol. Cells **119**, 26 (2013)

S. Klein, F. Finger, R. Carius, T. Dylla, B. Rech, M. Grimm, L. Houben, M. Stutzmann, Thin Solid Films **430**, 202 (2003)

J. Kocka, A. Fejfar, P. Fojtik, K. Luterova, I. Pelant, B. Rezek, H. Stuchlikova, J. Stuchlik, V. Svrcek, Sol. Energy Mater. Sol. Cells **66**, 61 (2001)

J. Kocka, A. Fejfar, H. Stuchlıkova, J. Stuchlık, P. Fojtık, T. Mates, B. Rezek, K. Luterova, V. Svrcek, I. Pelant, Sol. Energy Mater. Sol. Cells **78**, 493 (2003)

S. Komuro, Y. Aoyagi, Y. Segawa, S. Namba, A. Masuyama, H. Okamoto, Y. Hamakawa, J. Appl. Phys. **55**, 3866 (1984)

M. Kondo, Sol. Energy Mater. Sol. Cells **78**, 543 (2003)

U. Kroll, J. Meier, P. Torres, J. Pohl, A. Shah, J. Non-Cryst. Solids **68**, 227–230 (1998)

A. Lambertz, T. Grundler, F. Finger, J. Appl. Phy. **109**, 113109 (2011)

A. Lambertz, F. Finger, B. Holländer, J.K. Rath, R.E.I. Schropp, J. Non-Cryst. Solids **358**, 1962 (2012)

A. Lambertz, V. Smirnov, T. Merdzhanova, K. Ding, S. Haas, G. Jost, R.E.I. Schropp, F. Finger, U. Rau, Sol. Energy Mater. Sol. Cells **119**, 134 (2013)

M. Ledinsky, L. Fekete, J. Stuchlik, T. Mates, A. Fejfar, J. Kocka, J. Non-Cryst. Solids **352**, 1209 (2006)

Y. Mai, S. Klein, R. Carius, et al., J. Non-Cryst. Solids **352**, 1859 (2006)

T. Matsui, M. Kondo, K. Ogata, T. Ozawa, M. Isomura, Appl. Phys. Lett. **89**, 142115 (2006)

T. Matsui, C.W. Chang, M. Kondo, K. Ogata, M. Isomura, Appl. Phys. Lett. **91**, 10211 (2007)

T. Matsui, C.W. Chang, T. Takada, M. Isomura, H. Fujiwara, M. Kondo, Sol. Energy Mater. Sol. Cells **93**, 1100 (2009)

T. Matsui, M. Kondo, Sol. Energy Mater. Sol. Cells **119**, 156 (2013)

J. Meier, R. Fluckiger, H. Keppner, A. Shah, Appl. Phys. Lett. **65**, 860 (1994a)

J. Meier, S. Dubail, R. Fluckiger, D. Fischer, H. Keppner, A. Shah, Proc. of 1st World Conference on Photovoltaic Energy Conversion (1994b), p. 409

J. Meier, P. Torres, R. Platz, S. Dubail, U. Kroll, J.A. Anna Selvan, N. Pellaton Vaucher, C. Hof, D. Fischer, H. Keppner, A. Shah, K.D. Ufert, P. Giannoulès, J. Koehler, Mater. Res. Soc. Symp. Proc. **420**, 3 (1996)

J. Meier, S. Dubail, J. Cuperus, U. Kroll, R. Platz, P. Torres, J.A.A. Selvan, P. Pernet, N. Beck, N.P. Vaucher, C. Hof, D. Fischer, H. Keppner, A. Shah, J. Non-Cryst. Solids **1250**, 227–230 (1998)

J. Meier, S. Dubail, S. Golay, U. Kroll, S. Fay, E. Vallat-Sauvain, L. Feitknecht, J. Dubail, A. Shah, Sol. Ener. Mater. & Sol. Cells **74**, 457 (2002)

T. Merdzhanova, J. Woerdenweber, W. Beyer, T. Kilper, U. Zastrow, M. Meier, H. Stiebig, A. Gordijn, J. Non-Cryst. Solids **358**, 2171 (2012)

J. MuKller, O. Kluth, S. Wieder, H. Siekmann, G. Schope, W. Reetz, O. Vetterl, D. Lundszien, A. Lambertz, F. Finger, B. Rech, H. Wagner, Sol. Ener. Mater. & Sol. Cells **66**, 275 (2001)

J. Müller, G. Schöpea, O. Klutha, B. Recha, V. Sittingerb, B. Szyszkab, R. Geyerc, P. Lechnerc, H. Schadec, M. Rusked, G. Dittmare, H.-P. Bochemf, Thin Solid Films **442**, 158 (2003)

Y. Nasuno, M. Kondo, A. Matsuda, Japn. J. Appl. Phys. **40**, 303 (2001)

J. Ni, Q. Liu, J. Zhang, J. Ma, H. Wang, X. Zhang, Y. Zhao, Sol. Energy Mater. Sol. Cells **126**, 6 (2014)

S. Nicolay, M. Despeisse, F.-J. Haug, C. Ballif, Solar Ener. Mater. & Sol. Cells **95**, 1031 (2011)

C. Niikura, M. Kondo, A. Matsuda, J. Non-Cryst. Solids **42**, 338–340 (2004)

C. Niikura, M. Kondo, A. Matsuda, Sol. Energy Mater. Sol. Cells **90**, 3223 (2006)

A. Pawlikiewicz, S. Guha, Mater. Res. Soc. Symp. Proc. **118**, 599 (1988)

S. Pillai, K.R. Catchpole, T. Trupke, M.A. Green, J. Appl. Phys. **101**, 093105 (2007)

A. Poruba, A. Fejfar, Z. Remes, J. Springer, M. Vanecek, J. Kocka, J. Appl. Phys. **88**, 148 (2000)

M. Python, O. Madani, D. Domine, F. Meillaud, E. Vallat-Sauvain, C. Ballif, Sol. Energy Mater. Sol. Cells **93**, 1714 (2009)

S. Ray, S. Mukhopadhyay, T. Jana, R. Carius, J. Non-Cryst. Solids **761**, 299–302 (2002)

B. Rezek, J. Stuchlík, A. Fejfar, J. Kočka, J. Appl. Phys. **92**, 587 (2002)

Y. Sobajima, S. Nakano, T. Toyama, H. Okamoto, S. Omae, T. Minemoto, H. Takakura, Y. Hamakawa, J. Appl. Phys. **101**, 103537 (2007)

T. Roschek, T. Repmann, J. Müller, B. Rech, H. Wagner, Proc. of 28th IEEE Photovoltaic Specialists Conference (IEEE, Anchorage, 2000), p. 150

H. Sai, H. Fujiwara, M. Kondo, Sol. Energy Mater. Sol. Cells **93**, 1087 (2009)

H. Sai, Y. Kanamori, M. Kondo, Appl. Phys. Lett. **98**, 113502 (2011)

H. Sai, K. Saito, M. Kondo, IEEE J. Photovoltaics **3**, 5 (2012)

H. Sai, K. Maejima, T. Matsui, T. Koida, M. Kondo, S. Nakao, Jap. J. Appl. Phys **54**(8S1), 08KB05 (2015)

A.V. Shah, J. Meier, E. Vallat-Sauvain, N. Wyrsch, U. Kroll, C. Droz, U. Graf, Sol. Energy Mater. Sol. Cells **78**, 469 (2003)

L. Sivec, B. Yan, G. Yue, J. Owens-Mawson, J. Yang, S. Guha, IEEE J. Photovoltaics **2**, 27 (2012)

V. Smirnov, A. Lambertz, B. Grootoonk, R. Carius, F. Finger, J. Non-Cryst. Solids **358**, 1954 (2012)

T. Söderström, F.-J. Haug, V. Terrazzoni-Daudrix, X. Niquille, M. Python, C. Ballif, J. Appl. Phys. **104**, 104505 (2008)

K. Söderströmn, G. Bugnon, F.-J. Haug, S. Nicolay, C. Ballif, Solar Ener. Mater. & Sol. Cells **101**, 193 (2012a)

K. Söderströmn, G. Bugnon, R. Biron, C. Pahud, F. Meillaud, F.-J. Haug, C. Ballif, J. Appl. Phys. **112**, 114503 (2012b)

P. Spinelli, V. E. Ferry, J. van de Groep, M. van Lare, M. A. Verschuuren, R. E. I. Schropp, .H. A. Atwater, and A. Polman, J. Opt. 14, 024002 (2012)

R.A. Street, Appl. Phys. Lett. **59**, 1084 (1991)

C. Strobel, B. Leszczynska, U. Merkel, J. Kuske, D.D. Fischer, M. Albert, J. Holovský, S. Michard, J.W. Bartha, Sol. Energy Mater. Sol. Cells **143**, 347 (2015)

H. Tan, L. Sivec, B. Yan, R. Santbergen, M. Zeman, A.H.M. Smets, App. Phys. Lett. **102**, 153902 (2013)

H. Tan, E. Moulin, F.T. Si, et al., Progr. in Photovoltaics: Res. and Appl. **23**, 949 (2015)

Y. Tawada, K. Tsuge, M. Kondo, H. Okamoto, Y. Hamakawa, J. Appl. Phys. **53**, 5273 (1982)

A. Terakawa, Sol. Energy Mater. Sol. Cells **119**, 204 (2013)

P. Torres, J. Meier, R. Fluckiger, U. Kroll, J.A.A. Selvan, H. Keppner, A. Shah, S.D. Littlewood, I.E. Kelly, P. Giannoules, Appl. Phys. Lett. **69**, 1373 (1996)

R. Tsu, J. Gonzalez-Hernandez, S.S. Chao, S.C. Lee, K. Tanaka, Appl. Phys. Lett. **40**, 534 (1982)

S. Usui, K. Kikuchi, J. Non-Cryst. Solids **34**, 1 (1979)

E. Vallat-Sauvain, C. Droz, F. Meillaud, J. Bailat, A. Shah, C. Ballif, J. Non-Crystal. Solids **352**, 1200 (2006a)

E. Vallat-Sauvain, A. Shah, J. Bailat, *Advances in microcrystalline silicon solar cell technologies* (Wiley, Chichester, 2006b), pp. 133–171

O. Vetterl, F. Finger, R. Carius, P. Hapke, L. Houben, O. Kluth, A. Lambertz, A. Mück, B. Rech, H. Wagner, Sol. Energy Mater. Sol. Cells **62**, 97 (2000)

O. Vetterl, M. Hulsbeck, J. Wolff, R. Carius, F. Finger, Thin Solid Films **427**, 46 (2003)

S. Veprek, V. Marecek, Solid State Electron. **11**, 683 (1968)

O. Vettea, A. Groß, T. Jana, S. Ray, A. Lambertz, R. Carius, F. Finger, J. Non-Cryst. Solids **772**, 299–302 (2002)

D.L. Williamson, Sol. Energy Mater. Sol. Cells **78**, 41 (2003)

J. Woerdenweber, T. Merdzhanova, T. Zimmermann, A.J. Flikweert, H. Stiebig, W. Beyer, A. Gordijn, J. Non-Cryst. Solids **358**, 2183 (2012)

K. Yamamoto, A. Nakajima, M. Yoshimi, et al., Prog. in Photovoltaics: Res. and Appl. **13**, 489 (2005)

B. Yan, K. Lord, J. Yang, S. Guha, J. Smeets, J.-M. Jacquet, Mater. Res. Soc. Symp. Proc. **715**, 629 (2002)

B. Yan, G. Yue, J. Yang, S. Guha, D.L. Williamson, D. Han, C.-S. Jiang, Mater. Res. Soc. Symp. Proc. **808**, 575 (2004a)

B. Yan, G. Yue, J. Yang, S. Guha, D.L. Williamson, D. Han, C.-S. Jiang, Appl. Phys. Lett. **85**, 1955 (2004b)

B. Yan, G. Yue, J.M. Owens, J. Yang, S. Guha, Appl. Phys. Lett. **85**, 1925 (2004c)

B. Yan, C.-S. Jiang, C.W. Teplin, H.R. Moutinho, M.M. Al-Jassim, J. Yang, S. Guha, J. Appl. Phys. **101**, 033712 (2007)

B. Yan, G. Yue, L. Sivec, J. Yang, S. Guha, C.-S. Jiang, Appl. Phys. Lett. **99**, 113512 (2011)

B. Yan, G. Yue, L. Sivec, J. Owens-Mawson, J. Yang, S. Guha, Sol. Ener. Mater. & Sol. Cells **104**, 13 (2012)

B. Yan, G. Yue, J. Yang, S. Guha, Sol. Energy Mater. Sol. Cells **111**, 90 (2013)

L. Yang, L. Chen, J.Y. Hou, Y.M. Li, Mater. Res. Soc. Symp. Proc. **258**, 365 (1992)

J. Yang, A. Banerjee, S. Guha, Appl. Phys. Lett. **70**, 2975 (1997)

J. Yang, K. Lord, B. Yan, A. Banerjee, S. Guha, Proc. of 29th IEEE Photovoltaic Specialists Conference (IEEE, New Orleans, 2002), p. 1094

G. Yue, B. Yan, J. Yang, S. Guha, Appl. Phys. Lett. **86**, 092103 (2005)

G. Yue, B. Yan, G. Ganguly, J. Yang, S. Guha, Mater. Res. Soc. Symp. Proc. **910**, 29 (2006a)

G. Yue, B. Yan, G. Ganguly, J. Yang, S. Guha, C. Teplin, Appl. Phys. Lett. **88**, 263507 (2006b)

G. Yue, B. Yan, G. Ganguly, J. Yang, S. Guha, J. Mater. Res. **22**, 1128 (2007)

G. Yue, B. Yan, C.W. Teplin, J. Yang, S. Guha, J. Non-Crystal Solids **354**, 2440 (2008)

G. Yue, B. Yan, L. Sivec, T. Su, Y. Zhou, J. Yang, S. Guha, Mater. Res. Soc. Symp. Proc. **1426**, 33 (2012a)

G. Yue, B. Yan, L. Sivec, Y. Zhou, J. Yang, S. Guha, Sol. Energy Mater. Sol. Cells **104**, 109 (2012b)

X. Zhang, G. Wang, X. Zheng, C. Wei, X. Geng, S. Xiong, Y. Zhao, Sol. Energy Mater. Sol. Cells **95**, 2448 (2011)

X. Zhang, In OSA Light Energy Nanostructures and Advanced Materials for Photovoltaics (PV), Leipzig (2016)